Surface Science Reports xxx (xxxx) xxx

Contents lists available at ScienceDirect

Surface Science Reports

journal homepage: www.elsevier.com/locate/surfrep

Graphene grown on transition metal substrates: Versatile templates for organic molecules with new properties and structures

Cristina Díaz [a,*], Fabián Calleja [b], Amadeo L. Vázquez de Parga [b,c,e], Fernando Martín [b,d,e]

[a] Departamento de Química Física, Facultad de CC. Químicas, Universidad Complutense de Madrid, 28040, Madrid, Spain
[b] Instituto Madrileño de Estudios Avanzados en Nanociencia (IMDEA-Nanociencia), Cantoblanco, 28049, Madrid, Spain
[c] Departamento de Física de La Materia Condensada, Módulo 3, Universidad Autónoma de Madrid, 28049, Madrid, Spain
[d] Departamento de Química, Módulo 13, Universidad Autónoma de Madrid, 28049, Madrid, Spain
[e] Condensed Matter Physics Center (IFIMAC), Universidad Autónoma de Madrid, 28049, Madrid, Spain

ARTICLE INFO

Keywords:
Graphene on metals
Organic molecules
Geometrical properties
Electronic properties

ABSTRACT

The interest in graphene (a carbon monolayer) adsorbed on metal surfaces goes back to the 60's, long before isolated graphene was produced in the laboratory. Owing to the carbon-metal interaction and the lattice mismatch between the carbon monolayer and the metal surface, graphene usually adopts a rippled structure, known as moiré, that confers it interesting electronic properties not present in isolated graphene. These moiré structures can be used as versatile templates where to adsorb, isolate and assemble organic-molecule structures with some desired geometric and electronic properties. In this review, we first describe the main experimental techniques and the theoretical methods currently available to produce and characterize these complex systems. Then, we review the diversity of moiré structures that have been reported in the literature and the consequences for the electronic properties of graphene, attending to the magnitude of the lattice mismatch and the type of interaction, chemical or physical, between graphene and the metal surface. Subsequently, we address the problem of the adsorption of single organic molecules and then of several ones, from dimers to complete monolayers, describing both the different arrangements that these molecules can adopt as well as their physical and chemical properties. We pay a special attention to graphene/Ru(0001) due to its exceptional electronic properties, which have been used to induce long-range magnetic order in tetracyanoquinodimethane (TCNQ) monolayers, to catalyze the (reversible) reaction between acetonitrile and TCNQ molecules and to efficiently photogenerate large acenes.

1. Introduction

Although there is a general consensus in the scientific community that 2004 is the year of birth of graphene science, promoted by the pioneering work of Geim and Novoselov [1], evidence of graphene formation on metal surfaces goes back to 1969 [2], although at that time it was called monolayer of graphite or carbon monolayer. In standard preparation procedures, these carbon monolayers originate from the segregation of bulk carbon impurities to the metal surface during annealing at high temperatures in Ultra-High Vacuum (UHV) conditions [3]. The seggregated carbon impurities can nucleate as graphitic monolayers on almost any transition metal [4]. For instance, a graphitic monolayer was experimentally observed on nickel via Auger electron spectroscopy (AES) [5]. This graphitic phase was found to persist over a large range of temperatures [6,7]. In first studies performed in the 70's, a single graphite layer was observed experimentally on platinum via AES and low-energy electron diffraction (LEED) [8,9], and in rhodium via AES, LEED and thermal desorption spectroscopy (TDS) [10]. Since then and until 2004, this carbon segregation and the resulting carbonaceous or graphitic monolayers were widely observed as unexpected and/or unwanted by-products, preventing access to the originally devised surface or even poisoning some intended catalytic reactions. During the 80's and 90's, several experimental techniques were used to study the presence of these two-dimensional carbon phases [11]. For example, angle-resolved photoemission spectroscopy (ARPES)[1] was used to study carbon-induced two-dimensional energy bands on Ru(0001) [14,15]

* Corresponding author.
E-mail address: crdiaz08@ucm.es (C. Díaz).

[1] The development of ARPES allowed for the characterization of the Dirac cone on graphene grown on weakly interactioning substrates [12,13].

https://doi.org/10.1016/j.surfrep.2022.100575
Received 16 February 2022; Received in revised form 6 June 2022; Accepted 11 July 2022
Available online 18 September 2022

and also the decomposition of acetylene to graphitic and carbidic carbon, via desorption of hydrogen, on clean and K-covered Co(0001) [16]. This later phenomenon was also studied using X-ray photoelectron diffraction (XPD) and TDS. TDS was also used to reveal the graphitic monolayer formation on several iridium surfaces [17]. Photoemission energy-loss and ionization-loss spectroscopy techniques were used to study carbon overlayers on Ni(111) [18]; on Ni(100) a carbon monolayer was shown to decompose opening up free Ni sites when the temperature rises enough [19]. Scanning tunneling microscopy (STM) showed the formation of single and multiple carbon layers upon hydrocarbon decomposition on platinum [20,21], nickel [22,23], and ruthenium [24]. From the 80's, we also find the first theoretical descriptions [25–27], which showed, for example, the main role that nucleation and lateral diffusion may play in carbon segregation or the similarity between the binding configuration of graphitic monolayer on Ru(0001) and that of bulk RuC.

These first evidences of carbon aggregates formation on metal substrates triggered the interest on these systems. The purposeful growth of monolayer graphite films onto several substrates by Chemical Vapor Deposition (CVD) was also reported well before the isolation of graphene [27], but the degree of characterization of the films was hampered by the existing experimental limitations. Among the most studied systems in this period, we find monolayer-graphite grown on a nickel substrate. This system has been investigated using a wide range of experimental techniques, extended-energy-loss fine-structure spectroscopy [28,29], ARPES [30], LEED [31], reflection high-energy electron diffraction (RHEED), and Li^+-ion scattering spectroscopy [32], revealing the strong interaction between the graphite monolayer and the nickel surface, due to the hybridization of the π state of the former with the *d* orbitals of the latter, and the single graphite plane slightly expanded with respect to the graphite bulk. The characterization of graphite monolayers on several metal surfaces was performed using STM [33], atomic force microscopy (AFM), and point contact microscopy [34]. Beyond the atomic and electronic structure, the spatial modulation of the local surface potential [35] and the phonon dispersion [36–38] of the graphite monolayer were also investigated. At that time, there were also studies related to intercalation of atoms [39–43] and even molecules [44,45] between the graphite monolayer and the metal surface. These studies showed, for example, the great thermal stability of the intercalated elements, which remain underneath the monolayer upon heating up to the annihilation temperature of graphite [43]. In the case of graphite monolayer on Ni(111), it was shown, analyzing the surface phonon dispersion, measured via high-resolution electron energy loss spectroscopy (HREELS), that the intercalation of noble-metal atoms, such as Cu [40,41] and Ag [42], weakens the strong interaction between the graphite monolayer and Ni(111) due to the small charge transfer from the noble-metal atoms to the π-state of graphite. On the other hand, the intercalation of rare earth atoms [41] also decouples the graphite monolayer from the Ni substrate, but in this case as a consequence of the strong interaction between the graphite monolayer and the rare-earth atoms.

However, the real interest of the scientific community for these monocrystalline graphitic films, since then called openly graphene, began in 2004 when Novoselov et al. [1] showed that such material is stable under ambient conditions. Since then the topological and electronic properties of graphene have been widely studied. Due to its unique electronic properties, graphene has been considered as one possible candidate for substitution, and/or as a complement, to Si-based electronics for future applications including spintronics, nanomagnetoelectronics, and optoelectronics. But, to develop this potential, one should be able to control the type and the concentration of charge carriers on graphene. The adsorption of organic molecules on graphene/metal (hereafter Gr/metal for short) substrates, specially of aromatic molecules, provides an opportunity to tune the electronic properties of graphene in a desired way. But to achieve such a control, a detailed understanding of the organic molecule/graphene interaction, and the charge transfer mechanism that governs it, is required. This explains the efforts invested in studying and analyzing the basic properties that rule the interactions within these systems (see Refs. [46–49] and refs. therein). As a result of this commendable effort, it has been found that in some cases organic molecules can adsorb weakly on freestanding graphene or graphene absorbed on a 6H–SiC(0001) semiconducting surface [50–52] allowing, for example, the formation of an organic monolayer but conserving at the same time the properties of the pristine molecules [53–55]. In addition, the presence of functional groups [56] or the modification of graphene thickness [57] may tune the magnitude of the π-π interactions between graphene and the organic molecules. In some cases, the adsorption of organic molecules, isolated or as monolayer, may induce graphene functionalization [58], including both p-type (holes) or n-type (electrons) doping. For example, tetracyanoquinodimethane (TCNQ) -see Fig. 6 (b), tetrafluoro-tetracyanoquinodimethane (F4-TCNQ) -see Fig. 6 (c), tetracyanoethylene (TCNE), 2,3,-dichloro-1, 4-benzoquinone (DDQ), and perylene-3,4,9,10-tetracarboxylic-3,4,9, 10-dianhydride (PTCDA) -see Fig. 6 (e)- induce p-doping of freestanding graphene and of graphene grown on 6H–SiC(0001) [59–67], while 4-amino-2,2,6,6-tetramethyl-1-piperridinyloxy (4-amino--TEMPO), tetrathiofulvalene (TTF), perylene-3,4,9,10-tetracarboxylic-3, 4,9,10-dianhydride-diimide (PTCDI) -see Fig. 6 (d)-, and vanadyl-phthalocyanine (VOPc) induce n-doping [63,64,66–68]. Accordingly, the co-adsorption of donor and aceptor molecules opens the possibility to impose a smart control of the electronic properties of graphene [63,69,70]. The adsorption of organic molecules on graphene may also lead to controllable magnetic properties [71], or can be used to build nano-patterns as template for creating, in a controlled manner, organic molecular structures [72].

On the other hand, the adsorption of graphene on metal substrates, thanks to the large variety of moiré patterns resulting from the graphene-metal lattice mismatch [73], opens new possibilities to the design and growth of increasingly complex systems with well-defined structural and electronic properties. These moiré patterns, which also depend on the strength of the chemical bonding at the graphene-metal interface [74], are very promising and versatile templates where molecules can get adsorbed following the moiré periodicity, thus modulating, for example, the doping of the systems in the desired manner. Furthermore, the presence of graphene between the metal and the molecule inhibits or modulates the hybridization between the frontier orbitals allowing for the tuning, but also for a precise characterization, of the electronic and magnetic properties of the molecules. These functionalities of organic molecules/Gr/metal-substrate systems may play an important role in the future development of a variety of molecular-based electronic devices, such as organic solar cells, light emitting diodes and field-effect transistors.

We start our review by briefly describing the most important experimental techniques employed to prepare and analyze these kind of systems, and the theoretical tools, mostly based on density functional theory (DFT), employed to account for the experimental observations, paying special attention to the shortcomings and the strategies proposed to overcome them. Subsequently, in section 4, we briefly describe the interactions, weak and strong, that lead to the formation of the different moiré structures, focusing on Gr/Ir(111) as an example of a weak interaction system, and on Gr/Ru(0001), as an example of a strong interaction system. We also discuss briefly the effect on the graphene moiré properties of the intercalation of metal atoms between graphene and the metallic substrate. Finally, in section 5, we discuss the interaction of organic molecules with Gr/metal substrates, and the one-dimensional (1D) and two-dimensional (2D) organic structures that can be formed, as well as the new properties exhibited by these organic molecule/Gr/metal systems. We pay special attention to the prototype system TCNQ/Gr/Ru(0001) for which new and surprising properties have been found. For a more thorough and comprehensive review of Gr/metal structures, the moiré structures formed as a result of the local variations of the binding between graphene and transition metal

surfaces, and how these variations are reflected in the electronic structure of the template, the reader is invited to read the review by Wintterlin and Bocquet [73]. Readers interested in a more in-depth knowledge of the electronic properties of Gr/metal transition systems, including graphene with defects and graphene nanoribbons, are invited to read the review by Batzill [75].

2. Experimental techniques

The concept of 'modern surface science' as the study of surfaces down to the atomic or molecular level can be traced back to the 1950s when, as a consequence of the space race, UHV technologies were vastly developed [76]. UHV provided the needed environment in order to keep surfaces atomically clean for hours or days and hence a myriad of measurement and growth techniques started to develop at that time. Nowadays we have countless surface science techniques at our disposal and some of them, the ones that are more closely related to the present review, are the subject of this chapter. In section 2.1 we will briefly describe the techniques that made possible the preparation and characterization of the samples under discussion, while in section 2.2 we will give a more detailed overview about some aspects of the measurement technique employed to obtain the main experimental results, namely STM/STS.

2.1. Sample preparation

Experimental surface science can be viewed as a combination of sample preparation and characterization techniques under UHV conditions, which developed side by side relying on the feedback provided by each other. Preparation techniques usually (in the context of the present review) start from a single crystal surface cleaned by cycles of noble gas ion sputtering and annealing. Then, the pristine surface can be exposed in UHV to almost any combination of atoms or molecules either from solid (sublimation), liquid (evaporation) or gas sources in what is commonly known as CVD. Well known examples of this, are the growth of graphene on transition metals [75] or the growth of 2D transition metal dichalcogenides [77].

Regarding the particular case of the deposition of molecules under UHV, special attention has to be paid to their possible fragmentation, either intended or unintended. The reason is that the most common pressure sensors (usually of the Bayard-Alpert type) and residual gas analyzers do produce molecular fragments and radicals that can reach the sample surface. It is often the case that these fragments are more reactive than the parent molecule and they might end up playing a major role in the experiment. In fact, this can be taken to our advantage, as it was recently demonstrated for the covalent functionalization of graphene via molecular radicals produced in this way [78].

Along with preparation, characterization techniques provided information about the surface atomic structure, chemical composition and even electronic band structure, to name a few. Regarding surface atomic structure, the most commonly employed technique is LEED. In a LEED experiment, an electron beam in an energy range from 20 to 500 eV is focused on the sample surface while the diffracted electrons are projected onto a phosphorus coated screen [79]. The purpose of the low energy range is twofold: on the one hand, the electron wavelength is of the order of the atomic lattice constant and, hence, the first order diffraction angles are large enough to be clearly resolved on the screen. On the other hand, the electron mean free path inside the sample falls near the minimum of the universal curve, providing sensitivity to the first few atomic layers only, i.e. surface sensitivity. In this way LEED provides direct access to the surface atomic reciprocal lattice, allowing one to determine its crystalline quality as well as the presence of reconstructions, rotational domains or moiré patterns. This is especially important in metal supported graphene systems where both the rotation angle of graphene and the moiré pattern, resulting from the lattice mismatch towards the substrate, play a major role in the final properties of the surface, as it will become evident in the following sections. In Fig. 1 b, we show a typical LEED pattern obtained for Gr/Pb/Ir(111), i.e., a Pb intercalated Gr/Ir(111) system.

Regarding chemical composition, two usual techniques are AES and XPS spectroscopies [80]. Both techniques rely on the formation of core-level electron vacancies by either high energy electron impact (AES) or the photo-electric effect resulting from illumination with X-rays (XPS). AES is based in the analysis of the energy spectrum of Auger electrons, i.e. electrons that are emitted as a result of the de-excitation of an outer shell electron to occupy the core-level vacancy. The energy of the Auger electrons depends exclusively on the energy distribution of electronic levels in the parent atom which, in turn, is determined by its chemical identity. XPS, on the other hand, is based on the analysis of the photo-emitted electrons, whose kinetic energy can be related to their original binding energy inside the parent atom. Although the issue of how they exactly relate is far from trivial [81], the binding energy can be ultimately linked to the chemical species. Surface sensitivity in both cases is provided by the energy of the emitted electrons (either Auger or photo-emitted) falling close to the minimum in the universal mean free path curve and, hence, AES and XPS give access to the surface chemical composition.

Actually, photo-emission spectroscopy is not only limited to X-rays as a source, it is also performed with ultra-violet (UPS) or sychrotron radiation, depending on the particular experiment. And, more importantly, not only the kinetic energy of the photo-emitted electrons can be measured, their trajectories can also be analyzed in ARPES [82,83]. It turns out that the emission angle can be related to the momentum of the initial electronic state and, hence, ARPES gives access to the electronic band structure of the surface. This is of particular interest in the context of metal-supported graphene where, by measuring directly the Dirac cones it is possible to determine the actual effective mass and doping of the system.

2.2. Sample analysis by STM/STS

As we pointed out in section 2.1, the surface science techniques developed up to the 80s gave great insight about both the atomic and electronic structure of surfaces but with a common drawback: they all are spatially averaged techniques, with a typical sampling size of the order of hundreds of nm. This situation changed dramatically in 1982 with the invention of STM by Binnig, Rohrer, Gerber and Weibel [84]. STM gave us access to the surface electronic structure with atomic resolution, but there are some key concepts that must be understood in order to fully exploit STM data, at least in what concerns the present review. We outline them briefly in the following paragraphs.

STM is based in the quantum mechanical principle of electron tunneling between two electrodes, one of them being the sample surface and the other a metallic tip mounted in a high precision scanning system. The main operating principle is that the vertical position of the tip is controlled in such a way that a reference tunneling current is established and maintained while, at the same time, a lateral scanning action is performed. This is the so called topographic constant current mode, and the resulting z(x,y) maps are called STM topographic images. In Fig. 1 c, we show an example of STM topographic image for Gr/Pb/Ir (111).

In the low temperature limit, following the s-wave approximation introduced by Tersoff and Hamann in 1983 [85,86] and generalized for the finite bias voltage case [87], the tunneling current can be expressed as:

$$I|_{T\to 0} \propto \int_0^{eV_b} \mathrm{d}E\, \rho_t(E-eV)\, \rho_s(\vec{r_t}, E) \tag{1}$$

where V_b is the bias voltage applied to the sample, ρ_t is the Density of States (DOS) of the tip and $\rho_s(\vec{r_t})$ is the local density of states (LDOS) of the sample evaluated at the tip position $\vec{r_t}$.

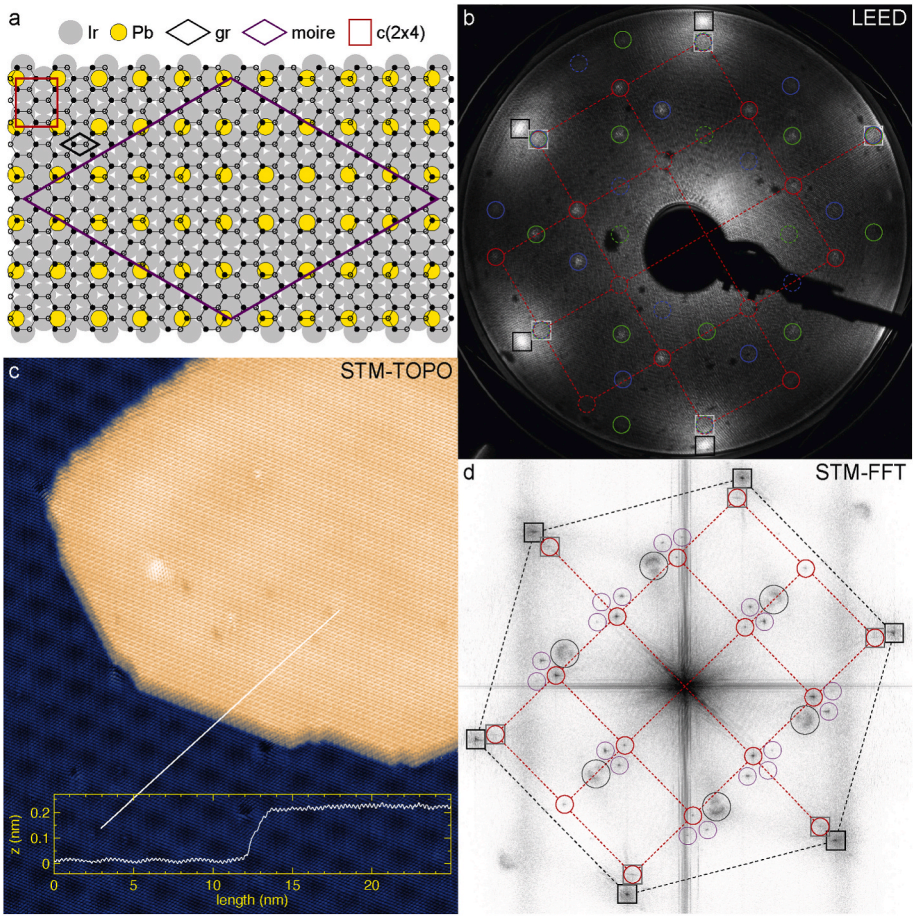

Fig. 1. (Color online) Structure of a lead intercalated Gr/Ir(111) system, determined by LEED and STM. a) Ball model of the Gr/Pb/Ir(111) system, as determined from the LEED and STM analysis presented in the following panels. Lead atoms form a c(2 × 4)-2Pb structure whose unit cell is represented by the red rectangle. This structure presents three equivalent rotational domains according to the three possible orientations of the lead lattice with respect to the neighboring graphene and iridium lattices. b) LEED pattern from an 80% intercalated Gr/Pb/Ir(111) surface. Black and grey squares mark graphene and iridium spots, respectively. These spots together with the absence of any arc at the radius corresponding to graphene indicate that both lattices are perfectly aligned, as represented in the ball model of panel a. Red, green, and blue circles mark the spots coming from the lead interlayer, which are consistent with the presence of three rotational domains of the c(2 × 4) structure presented in panel a, hence the three different colors employed. The c(2 × 4) lattice is higlighted with dashed lines for the case of the red domain, as a visual aid. This scenario is confirmed by the STM data presented in the following panels. c) STM topographic image acquired on a 20% intercalated Gr/Pb/Ir(111) sample. The image presents two regions, a pristine Gr/Ir region coming from the bottom left corner (blue tones in the color scale) with a lead interlayer entering from the upper right corner (yellow tones in the color scale), both of them atomically resolved. As indicated by the height profile presented in the lower inset, graphene's atomic lattice is the most prominent periodicity detected both in the pristine and in the intercalated regions, with a difference in apparent height consistent with the thickness of a single lead inter-layer. d) Fourier Transform of a low voltage STM image acquired on a single domain island similar to the one presented in panel c. Black and grey squares signal graphene and Ir spots respectively. The single domain, Pb-derived spots are highlighted by the red circles and red dashed lines, as in the case of the LEED pattern of panel b. Some satellites of the Gr-Ir moiré pattern arising from the lead spots are also present, and marked with purple circles. Finally, due to the STM imaging conditions, some intervalley scattering features appear at the corners of the surface Brillouin Zone of graphene, which are highlighted by black circles. (For interpretation of the references to color in this figure legend, the reader is referred to the Web version of this article.)

According to eq. (1), and assuming an ideal one-atom tip, an STM topographic image is just a constant LDOS profile for states inside the energy window defined by the bias voltage, where the distance between the LDOS profile and the surface atomic plane is defined by the combination of bias voltage and set-point tunneling current. Therefore, it is important to remind that STM is ultimately sensitive to the local electronic structure and that STM topographs are only indirectly related to the actual topography of the sample. This has important consequences that we would like to emphasize.

Let us begin with the case of an atomic resolution STM image. In this case, we are tuning electronic states localized around the surface atoms and, hence, the topo image could in principle be interpreted as a simple map of the atomic positions. Note however that, although the atomic periodicity would clearly be probed in this case, the exact determination of the atomic positions within the STM image is far from trivial, especially when more than one atomic species is present [88]. In addition, if the electronic structure of a given atom is modified for whatever reason (e.g. the formation of a new covalent bond), its signature in the topo image will be completely different, even if its actual position is roughly the same. Interestingly, this can be taken to our advantage, as it will become apparent further into the present review.

Another interesting case scenario is when imaging adatoms or molecules adsorbed on the surface. In this case, the energy window defined by the bias voltage will determine, among other things, if a given Molecular Orbital (MO) of the adsorbed system participates in the tunneling process. If this is the case, in principle, the molecule MO could be 'detected' in the topo image, although it has to be noted that tunneling into (or from) MOs might also trigger additional processes like vibrations, desorption, chemical reactions, etc. In the latter case, the tunneling process becomes inelastic and the lost energy is transferred to the adsorbate.

On the other hand, if no MO falls inside the energy window, the molecule would be 'invisible' to the STM, in the sense that its orbitals would not contribute to the constant LDOS profile followed by the tip. In this case, special attention has to be paid to the tip-sample interaction, since the tip-molecule distance could be dramatically reduced. Two possible scenarios arise here, depending on the molecule-surface interaction: if the molecule is physisorbed on the surface (weak molecule-surface interaction) then it could be easily swept away by the scanning action of the tip, which is often the case. On the contrary, if the molecule is chemisorbed, it could 'withstand' the scanning action of the tip. In this scenario, the only signature of the molecule would be the change in the substrate electronic structure inside the given energy window. In the example mentioned before of a molecule covalently bound to a single substrate atom, the result would be an atomic resolution image of the substrate exhibiting an atom 'different' from the rest.

The case scenarios mentioned so far emphasize that, even in the topographic mode, STM is ultimately sensitive to the electronic structure. This characteristic is further exploited in the so called spectroscopic mode, or Scanning Tunneling Spectroscopy (STS). In STS, the tip is usually held at a fixed position over the sample while an $I(V)$ curve (or more often its derivative) is recorded. Assuming a constant tip DOS in the energy window defined by the bias voltage, from eq. (1) follows:

$$\frac{dI}{dV}(V) \propto \rho_s(\vec{r_t}, eV) \approx \rho_s(\vec{r_s}, eV)\,\mathcal{T} \tag{2}$$

where $\vec{r_s}$ is the sample position and $\mathcal{T}$ is a transmission factor that takes into account the decay of the different states across the tunneling barrier. According to eq. (2), it turns out that the tunneling conductance can be related to the sample LDOS evaluated at the tip position. Therefore, STS gives access to the sample LDOS with atomic spatial resolution.

Up to now we have assumed the spin-degenerate case. However, if we add spin-polarization in both tip and sample, a similar analysis could be developed for both spin channels independently (assuming that spin-flip tunneling processes have a negligible contribution to the tunneling current). The consequence of this is a dependency of the total tunneling current in the relative orientation of the local magnetization of the sample and the tip. This can be used to add magnetic sensitivity to STM, in a technique known as 'spin-polarized STM' [89].

The brief overview presented in the previous lines can help understanding the amazing development that STM (and other scanning probe techniques derived from it) has experienced over the past 40 years. From the original instrument devised in 1982 by Binnig and Rohrer [84], STM was quickly implemented in different experimental conditions including gases, liquids and UHV [90], reaching also cryogenic temperatures and external magnetic fields [91]. By its 10th anniversary, it had been already used in the study of surface reconstructions, adsorbates, charge density waves, superconductivity, phonons, magnetism, biology, electrochemistry, tribology or nanolitography, to name a few [92]. From this point, STM continued its development in many different areas, having a major role in the field of surface science [93] and, in particular, in the study of graphene [94]. From the instrumental point of view, nowadays it is possible to measure under UHV conditions at temperatures as low as 10 mK, attaining an energy resolution of the order of μeV [95].

3. DFT periodic boundary conditions simulations

Theoretical simulations are very useful, sometimes crucial, to understand and contextualize experimental measurements. In dealing with semi-periodic systems, such as molecule/Gr/metal systems, the use of DFT seems unavoidable nowadays in order to accurately simulate interactions between the different elements. These semi-periodic systems are usually studied using periodic boundary conditions (PBC) in all three space directions, although the system is only 2D periodic in the lateral surface directions because symmetry is broken in the normal direction.

To avoid this inconsistency, a supercell is defined in such a way that periodic images do not interact with each other along the non periodic direction. In defining these supercells, one has to determine the minimum number of metal layers needed to simulate the surface and size of the unit cell in the graphene/metal plane. In the case of a simple graphene layer adsorbed on a metal substrate, the unit cell taken into consideration is usually the moiré cell itself, even when the actual unit cell is larger or even infinite (incommensurate systems). Thus, for the Gr/Ni(111) system, due to the similar lattice constant values of Ni(111) and graphene, a (1×1) unit cell accounts for the whole periodicity [31], whereas for Gr/Ru(0001), due the lattice constant mismatch, the minimum size required is much larger. For the latter, the presence of a moiré pattern with a periodicity comprising several atomic lattices requires the use of a supercell containing a large number of atoms. In the case of graphene on Ru(0001) the unit cell is even larger than one would expect because as it was found by STM measurements the atomic lattices of graphene and ruthenium were rotated with respect to each other on the order of 0.3° [96,97]. Interestingly, this rotation is not observable by X-ray diffraction measurements [98–100] due to the superposition of rotational domains in the large sampling area of that technique. This rotation implies unit cell of the order of (133×133), corresponding to an effectively incommensurate system. The commonly accepted moiré structure for this system is (11.57×11.57)R0.3° [97]. Large moiré cells and non-zero rotation angles, in general, are needed to describe graphene/metal systems such as Gr/Ir(111) [101,102], Gr/Pt(111) [21,35] and Gr/Rh(111) [103]. For a more detailed analysis of this issue see Ref. [73] and references therein. When such large unit cells are employed, only a few k-points are needed to represent the Brillouin zone of the reciprocal lattice. In fact, for many simulations, only the Γ point is required. Different methods have been proposed to represent the Brillouin zone, such as the Monkhorst-Pack [104] and the Chadi-Cohen [105] schemes. Also several schemes have been proposed to describe the core electrons, from the computationally expensive norm-conserving pseudopotentials [106] to the more flexible and computationally cheaper nonlocal ultrasoft pseudopotentials (USPP) [107], and more recently the projector augmented wave method (PAW) [108]. Another important issue to face in performing PBC-DFT calculations is related to the description of the electronic wave function. The most extended method is the expansion of the wave function in terms of a discrete plane wave basis set; although the expansion should include an infinite number of terms, in practice, it is restricted to a finite number, which is defined by a cutoff energy value. This is the scheme used in some popular PBC-DFT codes such as QuantumExpresso [109], DACAPO [110] and VASP [111]. But the electronic wave function can also be expanded in orbital-like functions, as in ADF [112], CRYSTAL [113] or SIESTA [114].

In this theoretical context, we have to deal with the well-known inherent DFT shortcomings. For the interactions discussed in this review, the description of long-range forces (van der Waals -vdW-) is the key. First, because due to its π electronic cloud, graphene can be viewed as an extended aromatic molecule and, as in the case of those [115–120], the vdW forces play a prominent role on the adsorption energies and the geometry distortion of both the graphene and substrate as discussed below. Second, because of the presence of the organic molecules themselves, most of them containing also a π electronic cloud. In the context of this review, it should be taken into account that accurate descriptions of vdW forces based on costly embedded methods, in which a local interaction region is delimited aiming to accurately describe the interaction through high-level *ab-initio* simulations, such as the correlated wave function theory [121,122], cannot be applied for organic molecule/Gr/metal systems, because the graphene-metal interaction is itself periodic, and, therefore, its not possible to define a local interaction region. Thus, we have to rely on the different methods proposed to include long-range dispersion forces in DFT simulations.

3.1. Description of van der waals forces

As mentioned just above and widely discussed in Sec. 4 below, the interaction between a graphene monolayer and a metal surface is mainly ruled by vdW forces. Even in systems where graphene is chemisorbed, the role of vdW forces has been found to be very noticeable. An example of this phenomenon is given by the interaction of graphene with the Ru (0001) surface. For this system, it has been shown that the inclusion of vdW forces is crucial to understand and properly describe the moiré pattern measured experimentally. Whereas theoretical simulations based on standard DFT predict a corrugation between 1.5 and 1.7 Å [123–126], higher than the typical range of values found experimentally, between 0.15 and 1.5 Å [96,98,127,128], the inclusion of vdW forces lowers this value down to ≈ 1.2 Å [129] (see Fig. 2 top panels), showing the significant effect of vdW in a system where chemisorption is the dominant interaction. Thanks to the inclusion of vdW effects,

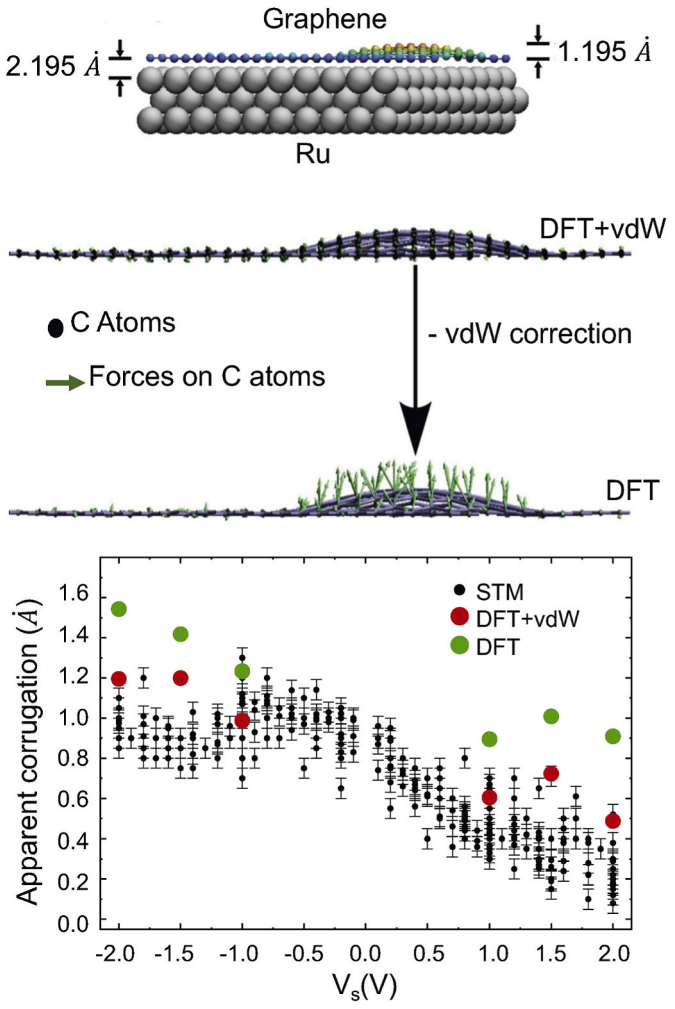

Fig. 2. (Color online) Top panel: Ground state geometry of (11 × 11) graphene adsorbed on a (10 × 10) Ru(0001) supercell calculated with DFT + vdW. Middle panel: Residual forces, represented by arrows, acting on the C atoms at the DFT and DFT + vdW level. Bottom panel: Apparent corrugation as a function of the bias voltage (V_s). Adapted from Ref. [129]. (For interpretation of the references to color in this figure legend, the reader is referred to the Web version of this article.)

theoretical simulations were able to accurately reproduce the apparent corrugation found in STM experiments as a function of the bias-voltage (see Fig. 2 bottom panel).

In the example given above, vdW interactions were taken into account through the empirical correction proposed by Grimme [130] (DFT + D). In this approach, the total energy E_{DFT+D} is written as $E_{DFT+D} = E_{DFT} + E_D$, where E_{DFT} is the self-consistent Kohn-Sham energy, commonly computed within the generalized gradient approximation (GGA), and E_D is a dispersion term given by:

$$E_D = s_6 \sum_{i=1}^{N_{at}-1} \sum_{j=i+1}^{N_{at}} \frac{C_6^{ij}}{R_{ij}^6} \frac{1}{1+e^{-\alpha(R_{ij}/R_0-1)}}, \tag{3}$$

where N_{at} represents the number of atoms, s_6 is a global scaling factor, R_{ij} the interatomic distance, R_0 the sum of atomic vdW radii, C_{ij} the dispersion coefficient, and α a scaling factor. A subsequent, improved variant to this approach (DFT + D2) was proposed in 2006 [131] aiming to provide better corrections at intermediate distances. This approach has been used, for example, to describe the strong chemical interaction between Graphene and Rh(111) [103,132]. However, the use of the DFT + D and, especially, the DFT + D2 approaches to study systems involving metal atoms can be questioned due to the lack of metallic systems in the benchmark series used to test their accuracy. A further improved (DFT + D3) was proposed in 2010 [133] incorporating atom-pairwise specific dispersion coefficients and cutoff radii computed from first principles. In this latter approach the dispersion term is written as $E_D = E_{2B} + E_{3D}$, where the two-body term (E_{2B}) is given by:

$$E_{2B} = -\sum_{ij} \sum_{n=6,8,\ldots} s_n \frac{C_n^{ij}}{R_{ij}^n} \frac{1}{1+6(R_{ij}/(s_{r,n}R_0^{ij}))^{-\alpha_n}}. \tag{4}$$

In this equation the first sum runs over all pairs, and C_n^{ij} represents the n_{th} order dispersion coefficient for the atoms pair ij. The three-body term (E_{3B}), on the other hand, is given by:

$$E_{3B} = -\sum_{ijk} \frac{C_9^{ijk}(3\cos\theta_I\cos\theta_J\cos\theta_K+1)}{(R_{ij}R_{jk}R_{ik})^3} \frac{1}{1+6(\overline{R}_{ijk}/(s_{r,3}R_0^{ijk}))^{-\alpha_3}}, \tag{5}$$

where the sum runs over all atom triples ijk in the system, $\overline{R}_{ijk}$ represents the geometrically averaged radii, and θ_I, θ_J, and θ_K are the internal angles of the triangle formed by R_{ij}, R_{jk}, and R_{ik}.

An alternative correction method, also based on empirical terms correction, was proposed in 2009 by Tkatchenko et al. [134]. There, the isotropic C_6^{ij} term is written as:

$$C_6^{ij} = \frac{3}{\pi}\int_0^\infty \alpha_i(iw)\alpha_j(iw)dw, \tag{6}$$

$\alpha_{i/j}$ being the frequency-dependent polarizability of i and j evaluated at imaginary frequencies. In this approach, the dispersion coefficient and the vdW radii are obtained from the mean-field ground-state electron density for molecules and solids. The method uses the electron density to compute the relative polarization of an atom in a molecule. A further improvement of this method was proposed in 2012 [135,136] making use of the self-consistent screening equation of classical electrodynamics, which allows one to take into account the many-body collective response of the substrate electrons. This correction has also been shown to reproduce accurately the Gr/Ru(0001) interaction, as well as the adsorption of organic molecules and their reactivity on this substrate [137].

Dispersion forces can also be taken into account using the method originally developed by Lundqvist et al. [138] and its different implementations [139–141], which include the effect of vdW forces adding a nonlocal electron correlation function (E_c^{nl}) to the standard exchange-correlation functional. So that

$$E_{xc} = E_{xc}^{GGA} + E_c^{LDA} + E_c^{nl} \tag{7}$$

where E_x^{GGA} is the exchange energy computed using the generalized gradient approximation and E_c^{LDA} the correlation energy computed within the local density approximation framework. E_c^{nl} is computed using a model response function. The actual form of this response function has been the subject of some controversy [142–144]. This method has been less used mostly due to its high computational cost, however the development of efficient algorithms [145] that speedup the calculations places this method at the same level of usefulness as those mentioned above.

3.2. STM simulations: the Tersoff-Hamann approach

From the DFT calculations, one can obtain directly or indirectly the main observables that can be measured experimentally or infered from the experimental results. A good agreement between theory and experiment allows for an accurate characterization of the system under study. For example, one can compute adsorption energies of a molecule

adsorbed on a substrate, graphene, metal or graphene/metal, simply as

$$E_{ads} = E_{molec+subs} - [E_{molec} + E_{subs}], \quad (8)$$

where $E_{molec\ +\ subs}$, E_{molec}, E_{subs} are the computed DFT energies for the complex molecule/Gr/metal substrate, the isolated molecule, and the complex Gr/metal substrate, respectively. In the case of a monolayer of molecules, one can compute the adsorption energy of the monolayer per molecule as

$$E_{ads}^{ML} = (E_{ML+subs} - [E_{ML} + E_{subs}])/m, \quad (9)$$

where E_{ML} and $E_{ML\ +\ subs}$ represent the computed DFT energy of the monolayer and the monolayer-substrate complex, respectively. This equation can be generalized for n monolayers as

$$E_{ads}^{nML} = (E_{nML+subs} - [E_{ML} + E_{(n-1)ML+subs}])/m. \quad (10)$$

One can also compute the lateral intermolecular interaction energy per molecule (E_{int}) as

$$E_{int} = (E_{ML} - mE_{molec})/m, \quad (11)$$

m being the number of molecules per supercell in the calculation.

Similarly, we can compute the electronic density, and the spline-density redistribution, $\Delta\rho(\vec{r})$, as the difference between the electronic density of the complex molecule/Gr/metal substrate and those of the isolated molecule and the complex Gr/metal substrate,

$$\Delta\rho(\vec{r}) = \rho_{mol+Gr+metal}(\vec{r}) - [\rho_{mol}(\vec{r}) + \rho_{Gr+metal}(\vec{r})]. \quad (12)$$

In Fig. 3, we show an example of electronic density redistribution for the case of a TCNQ (Fig. 3 A) and a F4-TCNQ (Fig. 3 B) molecule adsorbed on a Gr/Ru(0001) substrate. From these plots one can clearly see electron accumulation on the molecules and electron depletion on the substrate just below them, which is the signature of an electron charge transfer from the substrate to the molecule. It is possible to carry out a more detailed study of the charge redistribution [146] based on Bader formalism [147], through a topological analysis of the electron charge density.

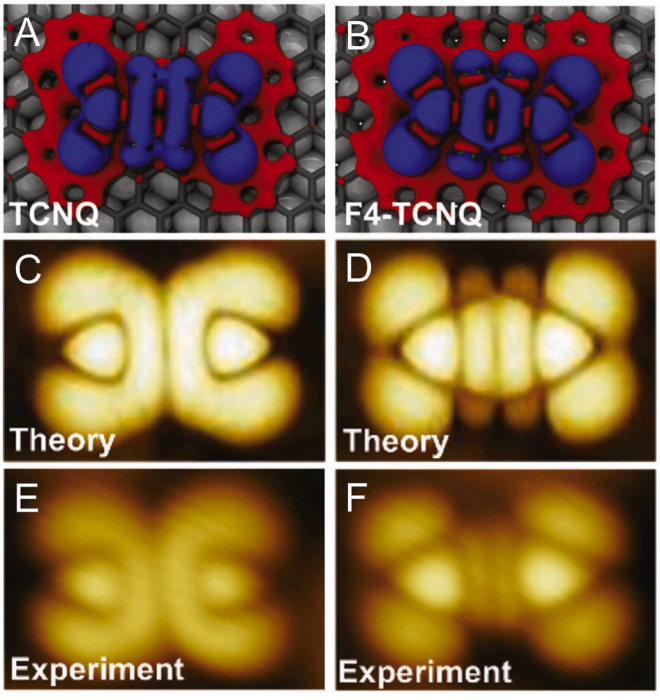

Fig. 3. (Color online) Top panels: Top view of the isosurface at a value of 1.0×10^{-4} e^{-}/Å, indicating the electronic density redistribution $\Delta\rho$ upon adsorption of TCNQ (A) and F4-TCNQ (B) on Gr/Ru(0001). Blue color indicates electron accumulation and red electron depletion. Middle panels: Simulated STM images of a TCNQ (C) and F4-TCNQ (D) adsorbed on Gr/Ru(0001) at negative bias voltage (integration range -0.3 eV $\leq E - E_F \leq 0.0$ eV). Bottom panels: High resolution STM topographies (3×3 nm^2) of a TCNQ (E) and a F4-TNCQ (F) adsorbed on Gr/Ru(0001) taken at -0.3 V ($I_t = 50$ pA). Adapted from [148]. (For interpretation of the references to color in this figure legend, the reader is referred to the Web version of this article.)

As discussed above, STM experimental images, which are the result of the electronic and topographic characteristics of the system, are a major observable in the study of the properties of all these systems. Therefore, it is desirable that they can also be simulated theoretically in order to extract useful information from them. A widely used formalism to simulate STM images from DFT outputs was the one proposed in the 80's by Tersoff and Hamann [85,86] (see also section 2.2). Within this formalism, the surface is described as accurately as possible whereas the STM tip is modeled as a simple locally spherical potential well. This latter approximation allows to write the tunneling current, based on Bardeen's formalism [149], as

$$I \propto \sum_n |\varphi_n(\vec{r}_0)|^2 \delta(E_n - E_f), \quad (13)$$

where the right hand side of this equation represents the surface local density of states (LDOS) at the Fermi energy (E_F). Thus, the STM image represents a contour map of constant surface LDOS. The use of a spherical symmetry on the single-orbital tip is the major restriction in this approach, although as shown in Ref. [150] the original Tersoff-Hamann formalism can be extended to consider p-like and d-like orbitals.

Despite, and thanks to, its simplicity, the Tersoff-Hamman formalism has been widely used to simulate STM images of molecules adsorbed on Gr/metal surface systems. In Fig. 3C and D, we show two examples of simulated STM images of TCNQ and F4-TCNQ adsorbed on Gr/Ru (0001). These simulated images, representing the LUMO of the molecules, resemble pretty much the experimental counterpart STM images (Fig. 3 E and F).

At this point, it is worth mentioning that the Tersoff-Hamann approach does not take into account the image potential, which modifies the interface tip-sample barrier. Neglecting this effect may affect the tunneling currents and, therefore, the STM images. To overcome this shortcoming, when necessary, one can rely on Green's function density functional formalisms (see Refs. [151,152] and Refs. therein).

4. Graphene on transition metals

Nowadays, epitaxial graphene on metal surfaces is routinely prepared by surface decomposition of hydrocarbon molecules. In some cases, the precursor molecules are adsorbed on the metal surface at room temperature and annealed to decompose them [20], or directly decomposed on the hot metal surface [24]. In both cases the growth of the graphene layer is a self-terminating process and the growth of a second layer and further is very difficult. This is easily understood if we consider the catalytic role of the hot metal surface for the decomposition of the carbon-containing molecules. The registry and interaction between the graphene overlayer and the metallic substrate varies in strength depending on the electronic properties of the metal and the lattice parameter mismatch [4].

4.1. Registry with the substrate: moiré patterns

The growth of epitaxial graphene monolayer by soft CVD under UHV conditions has been achieved on many single crystal metal substrates with hexagonal symmetry, such as Ir(111) [101,102,153,154], Ru (0001) [155–161] polycrystalline Ru [162], Pt(111) [163,164], Ni(111) [165], Cu(111) [166], Rh(111) [126], Re(0001) [167] or Co(0001)

[168,169].

The difference in lattice parameter between graphene (0.246 nm) and the different metal substrates with lattice constants ranging from 0.249 nm for Ni(111) up to 0.277 nm for Pt(111) causes the appearance of moiré patterns with lateral periodicities in the range of a few nanometers [170]. Graphene on Ni(111) and Co(0001) are the exceptions because their lattice mismatch is small enough to be accommodated by elastic deformation of the lattices a (1 × 1) structure is formed. The bonding interaction between the graphene overlayer and the metallic substrate also varies as demonstrated by the energy position and structure of the C_{1s} core levels measured by means of XPS [171].

In the case of graphene grown on strongly interacting substrates, such as Ru(0001), a single domain of the epitaxial graphene monolayer covers uniformly the substrate over lateral distances larger than several microns, reproducing the surface steps, dislocations and other structural defects [96,154,158]. Fig. 4 A shows that a monolayer of graphene on Ru(0001) presents a triangular periodic array of bumps originated from the moiré pattern with an average separation of around 3 nm. Marchini and co-workers [155] proposed a (11 × 11) superstructure with respect to the substrate based on STM and LEED measurements. Martoccia et al. [98], based on a fit to surface X-ray diffraction data, proposed a larger (23 × 23) supercell that takes into account the small buckling and lateral relaxations in the first ruthenium layer induced by the strong interaction with the graphene overlayer and the registry between the graphene and the second ruthenium layer. As mentioned before, due to a small rotation of the graphene layer with respect to the ruthenium substrate, of the order of 0.3° [96], the actual unit cell is way larger, pointing towards an effectively incommensurate system, with a currently accepted moiré cell of (11.57 × 11.57)R0.3° [97]. However, all the important features of this surface are present in the theoretical models by simply taking an unrotated (11 × 11) unit cell, as shown by simulations performed based on standard DFT [123] and later on by improved simulations based on vdW-DFT [129]. Fig. 4 B shows a scheme of such unit cell, the color code indicates the relative height of the carbon atoms. Depending on the registry of the graphene honeycomb ring with respect to the ruthenium atoms, we can distinguish four areas: atop, FCC, HCP and bridge (area between the FCC and HCP regions). In the atop areas no carbon atoms are placed on top of the Ru atoms contrary to the FCC and HCP areas where carbon atoms from one of the triangular sublattices of graphene are placed just above a Ru atom. The carbon atoms located on top of Ru atoms are chemically bonded with the substrate [123,125,129].

Moiré superstructures with similar periodicities have been reported for graphene on metallic substrates where the interaction is weak, e.g. Pt (111) [20,21,163] or Ir(111) [101,102], although in these cases the weakness of the interaction facilitates the formation of several rotational domains of graphene giving as result moiré superstructures with different periodicities [153]. The number of different rotational domains can be controlled, to some extent, adjusting the growth conditions during the CVD process. For Gr on Ir(111), when the graphene film is grown at low temperature, the film shows several domains with rotational misorientations [153]. On the contrary, when the graphene film is prepared by ethylene decomposition at high temperatures, well ordered domains forming a moiré superstructure with an incommensurate periodicity of 9.32 Ir lattice constants and a small vertical corrugation are formed [101,102,153,154]. The STM image in Fig. 4C shows the perfect order of the hexagonal moiré superstructure over the whole image. The graphene domains cover several terraces like a carpet, keeping the structural coherency through the substrate steps. The resulting moiré presents a registry similar to that of the graphene/Ru (0001) system, as can be seen in Fig. 4 D. For instance, in the atop areas, a honeycomb carbon ring is centered above an iridium atom. In the other areas, a carbon atom sits on top of an iridium atom, situating its three neighbors in threefold hollow sites on the Ir(111) surface. These areas correspond to the HCP and FCC regions, depending on the position of the honeycomb ring with respect to the second iridium layer. The main difference with respect to graphene on Ru(0001) is the lack of chemical bond between some carbon atoms and the Ir(111) surface.

4.2. *Effect of the substrate on the electronic structure of graphene on metals*

As mentioned above, XPS of the C_{1s} core levels reveals the differences in the electronic structure associated with different systems and, therefore, provides information on the bonding interaction between the metallic substrate and the graphene monolayer [171]. For strongly interacting metals, such as Ru(0001), two C_{1s} peaks appear in the spectrum, revealing the existence of two differently bonded C atoms. Accordingly, the graphene electronic structure is strongly modulated by the interaction with the metal and barely resembles that of free-standing graphene [96,129,156,172,173]. The corresponding ARPES spectra can be seen in Fig. 5 A. On the other hand, for weakly interacting substrates, such as Ir(111), only one C_{1s} level is present, indicating that all the carbon atoms are chemically equivalent. In this case, the graphene electronic structure, i.e. the Dirac cone, is only weakly modified with respect to free-standing graphene [12,13].

Graphene on Ru(0001) presents a spatial modulation in the chemical binding between the overlayer and the Ru(0001) substrate that gives rise to a periodic array of graphene regions of nanometer size displaying a different electronic structure. The experimental dI/dV spectrum, which is related to the LDOS, and theoretical calculations show that the occupied LDOS close to the Fermi level is larger on the high regions of the moiré, while the unoccupied LDOS is larger on the low areas of the moiré [156,157]. The modulation in the chemical bonding between graphene and ruthenium within the moiré unit cell modifies the surface dipole, which has a direct influence on the surface potential. This can be determined with high spatial resolution by measuring with STM the Field Emission Resonances (FERs) [174]. The energy position of the FERs, which are detected by STM when applying voltages larger than the work function of the sample, gives as result a spatial variation of the order of 0.25 eV in the surface potential values depending on the position in the moiré pattern [175]. All these electronic effects are behind the change in apparent corrugation of the moiré pattern in the STM images. A comparison between experimental results obtained for different experimental conditions and DFT calculations [129] allows one to disentangle the influence of several factors in measured STM images on this surface. As already discussed in Sec. 3.1, the apparent corrugation of the moiré pattern calculated by including (excluding) vdW corrections is in good (qualitative) agreement with that observed in STM experiments. The effect of vdW or dispersion forces plays an appreciable role in this system, since they are responsible for a reduction of 25% in the apparent corrugation of the moiré pattern [129]. The comparison between experiments and theoretical calculations allows for the identification of the electronic state responsible of the contrast inversion in the STM images for bias voltages higher than +2.6 V. This peak appears in the dI/dV spectra at +3.0 V only in the lower areas of the moiré. Its origin is traced back to the hybridization and confinement of a Ru(0001) surface resonance with the unoccupied density of states of graphene [175]. In summary, periodically rippled graphene on Ru(0001) behaves as a superlattice of modulated electronic properties.

As discussed above, graphene grown on Ir(111) is a prototypical case of weakly interacting substrate. Concerning the electronic structure, graphene on Ir(111) is close to freestanding graphene. The ARPES spectra of clean Ir(111) and Gr/Ir(111) along G-K-M show an unperturbed graphene Dirac cone as expected [12,13]. The main changes in the graphene Dirac cone due to the weak interaction with the Ir(111) substrate is the shift in energy of the Dirac cone due to the p-type doping as a result of the charge transfer between the overlayer and the substrate and the opening of minigaps in the cone due to the moiré superperiodicity that gives rise to the formation of replica cones at the Bragg planes [12], as can be seen in Fig. 5b,c. These features prove the long-range structural quality and uniformity of epitaxial Gr/Ir(111) that can be obtained when the CVD parameters are carefully adjusted [153].

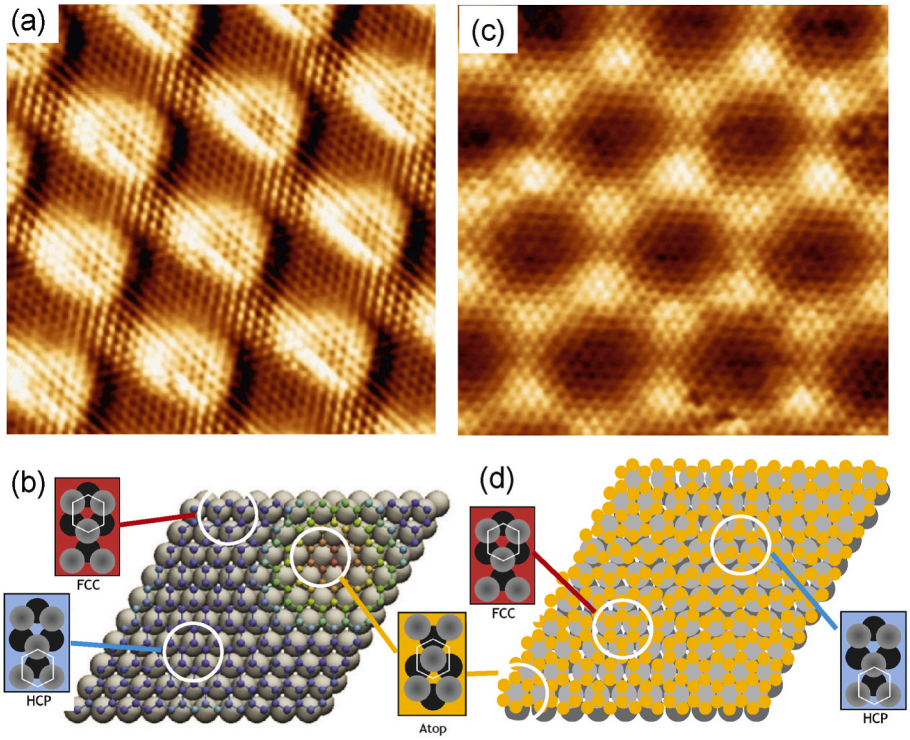

Fig. 4. (a) Atomically resolved STM image showing the moiré superperiodicity and the atomic corrugation on graphene grown on Ru(0001). Image parameters Vb = −1mV, It = 1 nA, 9 nm × 9 nm. (b) Ball model of the moiré unit cell of graphene on Ru(0001). The three stacking sequences present on the moiré unit cell are indicated. The white hexagon indicates the graphene honeycomb, the grey and black balls indicate the first and second Ru(0001) layer respectively. (c) Atomically resolved STM image showing the moiré superperiodicity and the atomic corrugation of graphene grown on Ir/(111). Image parameters Vb = 10 mV, It = 0.6 nA, 7 nm × 7 nm. (d) Ball model of the moiré unit cell of graphene on Ir(111). The three stacking sequences present on the moiré unit cell are indicated. The white hexagon indicates the graphene honeycomb, the grey and black balls indicate the first and second Ir(111) layer respectively.

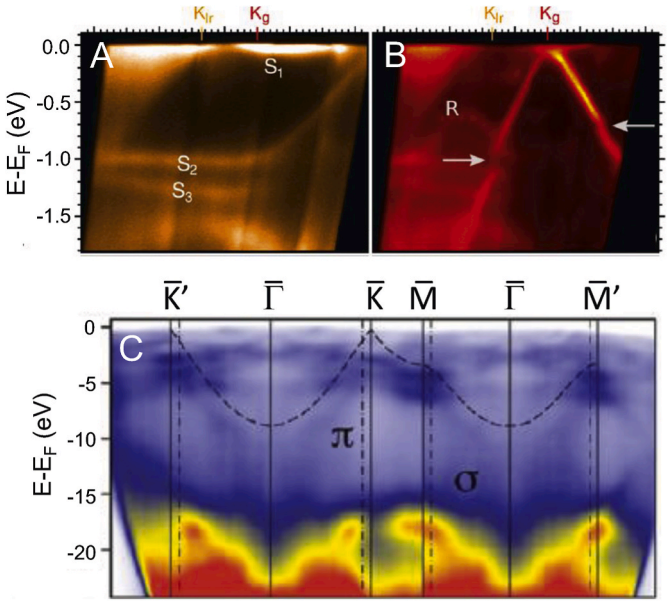

Fig. 5. (A) ARPES spectrum of clean Ir(111). The positions of K points of iridium and graphene are marked as KIr and Kg, respectively. S1, S2 and S3 are surface states. (B) ARPES spectrum of Ir(111) covered by graphene along the same azimuth as in (A). Horizontal arrows denote the minigap in the primary Dirac cone. A visible replica band is labeled as R. (C) Micro-ARPES band structure maps of epitaxial monolayer graphene. Dashed line: Band obtained from a tight-binding calculation for free-standing monolayer graphene. Adapted from [12,162].

4.3. *Further tuning via atom intercalation*

The growth of graphene on transition metals is a method to produce large areas of graphene with high crystallographic perfection, but the interaction with the substrate may change dramatically the electronic characteristics of graphene. Once the graphene overlayer is grown, a reduction of the interaction with the (catalytically reactive) metallic substrate can be obtained by intercalation of suitable atoms, which interact strongly with the metallic substrate, passivating it and, accordingly, allowing for recovering the pristine structure of the graphene overlayer. For instance, for graphene grown on Ni(111), the intercalation of Au [165], Ag [42] or Cu [176] has been used to decouple the graphene overlayer from the substrate. This decoupling effect of the intercalation has been shown to be successful even for a prototypical system with a strong interaction: Gr/Ru(0001). After intercalation of oxygen [177] or silicon [178], the structural corrugation of the graphene overlayer decreases strongly and graphene with free-standing characteristics (e.g. linear dispersing bands in the Dirac cone with Fermi velocity identical to Gr/SiO_2) is obtained.

The intercalation process can be also used to tailor the doping or other electronic properties of the graphene overlayer. In particular, the introduction of large spin-orbit coupling has been pursued in the past to make graphene an active component of spintronic devices or to generate a prototype 2D Topological Insulator [179]. In order to introduce a large spin-orbit coupling on graphene it is necessary to intercalate atoms with a large atomic number. It has been shown that the intercalation of Pb atoms between graphene and Ir(111) creates a monolayer of Pb atoms well ordered with respect to the Ir(111) surface and modifies the graphene electronic bands, shifting the Dirac point from p to n doping and producing a large spin splitting of the bands of graphene due to the local variations of the spin-orbit coupling introduced by the Pb atoms [13, 180].

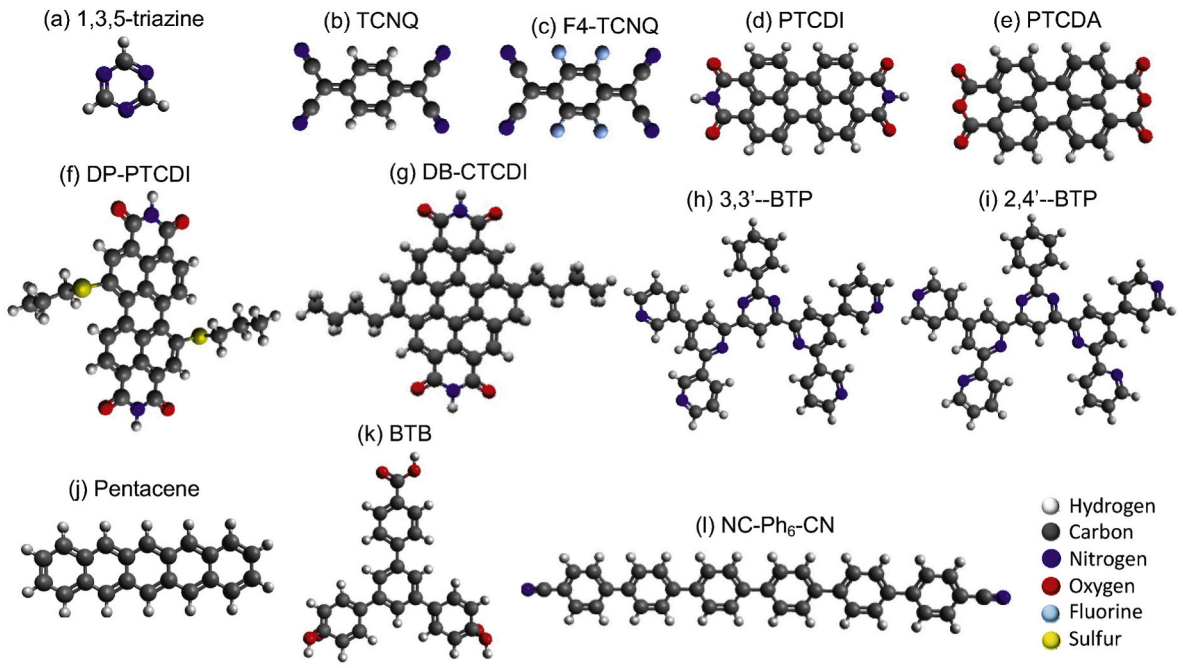

Fig. 6. (Color online) Molecular geometries of organic molecules, which have been found to adsorb on Gr/metal substrates. (a) 1,3,5-triazine; (b) 7,7,8,8-tetracyano-p-quinodimethane; (c) tetrafluoro-tetracyano-p-quinodimethane; (d) perylene-3,4,9,10-tetracarboxylic-3,4,9,10-dianhydride-diimide; (e) perylene-3,4,9,10-tetracarboxylic-3,4,9,10-dianhydride; (f) 1,7-dipropylthio-perylene-3,4:9,10-tetracarboxydiimide; (g)1,7-di(butyl)-coronene-3,4:9,10-tetracarboxylic acid bisimide; (h) 2-phenyl-4,6-bis-(6-(pyridin-3-yl)-4-((pyridin-3-yl)pyridin-2-yl)pyrimidine; (i) 2,4′-bis(terpyridine); (j) Pentacene; (k) 1,3,5-benzenetribenzoic acid; (l) para-hexaphenyl-dicarbonitrile. (For interpretation of the references to color in this figure legend, the reader is referred to the Web version of this article.)

5. Adsorption of organic molecules on graphene-metal substrate

As discussed in previous sections, the adsorption of graphene on a metal substrate modifies graphene's electronic and topological properties. This can be used in turn to modify the properties and/or chemical behavior of organic molecules when adsorbed on these systems, as compared to the adsorption on freestanding graphene or graphene adsorbed on insulators or semiconductors. In this section, we review existing work on adsorption of organic molecules on different graphene/metal substrates, both at the single-molecule level or in the form of two-dimensional arrays. At the end of the section, we will discuss in more detail a few singular examples for the Gr/Ru(0001) substrate, which has been widely used as a template for molecular adsorption due to its very especial properties, as discussed above.

5.1. Adsorption of single organic molecules on graphene/metal substrates

So far, most molecules deposited on Gr/metal substrates have a planar or quasiplanar structure, which maximizes their interaction with the substrate. For example, the 1,3,5-triazine molecule (see Fig. 10 (a)) adsorbed on Gr/Pt(111) [181] presents a diffusion barrier 20% higher than that of the molecule absorbed on a graphite surface [182], revealing the influence of the metal despite the weak coupling between graphene and Pt(111). For this system, the formation of fractal islands composed of ordered arrays with lattice constant slightly higher (≈2.5%) than that of graphene adsorbed on graphite surfaces has also been observed.

A systematic study of the adsorption of metal-phthalocyanines (MPc) -see Fig. 10 A-on Gr/Ni(111) has shown, in general, a weak coupling between the molecule and the substrate, mainly through its central metal atom, although the specific interaction strength and interaction channels were found to depend on the *d*-band filling [183,184]. For NiPc, CuPc and ZnPc, the interaction strength between graphene and the molecule is comparable to the π-π interaction between molecules, and the whole Pc molecule is efficiently decoupled from the underneath Ni surface. In contrast, for CoPc and FePc, the interaction is much stronger due to the strong coupling between the underneath metal substrate and the central metal atom of the molecule, in spite of the presence of graphene in between. In this case, the benzene rings of the molecules are completely decoupled from the substrate. The adsorption of FePc, NiPc, CoPc, CuPc and H_2Pc has also been studied on Gr/Ir(111) [185]. In this system, STM measurements and DFT simulations have found that the unsaturated dangling bonds located on the C atoms over the hollow sites of the Ir lattice induce a Diels-Alder concerted cycloaddition [186] reaction. Also related to phthalocyanine adsorption, X-ray absorption spectroscopy (XAS), and linear and magnetic circular dichroism (XLD and XMCD) have been employed to characterize the magnetic properties of two lanthanides bis-phthlocyanines with different magnetic anisotropy, $TbPc_2$ and $ErPc_2$, adsorbed on Gr/Ni(111) and on Gr/Au/Ni(111) (Au atoms intercalated between the Ni substrate and the graphene layer) [187]. This study showed that the antiferromagnetic signal measured for $TbPc_2$ adsorbed on Gr/Ni(111) disappears upon Au intercalation, whereas in the case of $ErPc_2$ the small antiferromagnetic signal measured upon adsorption on Gr/Ni(111) remains unaltered after Au intercalation. In the case of $TbPc_2$, the observed behavior was attributed to two possible causes: the increased distance between the $TbPc_2$ molecule and the magnetic substrate and the electronic decoupling between the graphene layer and the nickel substrate. In contrast, for $ErPc_2$, it seems to be a consequence of a significant contribution of the substrate magnetic dipolar field.

The role of metal substrates in tailoring the properties of graphene as a versatile template for the adsorption of organic molecules is clearly evidenced by the comparison of results obtained for F4-TCNQ and TCNQ adsorbed on Gr/Ir(111) and on Gr/Ru(0001). On Gr/Ir(111), TCNQ remains flat and neutral, whereas F4-TCNQ molecules coexist in flat and tilted forms [189]. The presence of two F4-TCNQ adsorption geometries

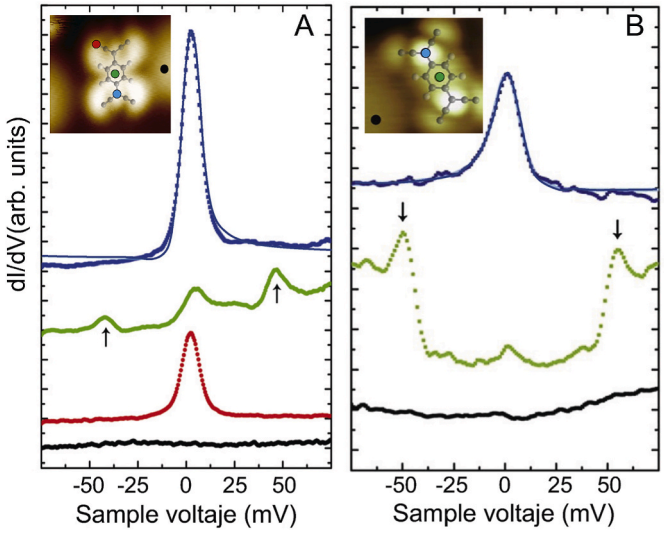

Fig. 7. (Color online) dI/dV spectra measured with the STM tip held on Gr/Ru (0001) and on different locations within the TCNQ (A) and F4-TCNQ (B) where the Kondo resonance is observed. The black arrows indicate the inelastic Kondo features. Adapted from Ref. [188]. (For interpretation of the references to color in this figure legend, the reader is referred to the Web version of this article.)

on Gr/Ir(111) has been explained in terms of work function modulation over the graphene moiré unit cell inducing site-selective charging of the molecule, so that on top and hcp sites (see Fig. 4 D) the molecule is adsorbed flat due to the lack of charge transfer, whereas on fcc sites the F4-TCNQ molecule gets charged and undergoes a strong structural relaxation. The charge transfer to the molecule has been evidenced by the presence of a Kondo resonance in the corresponding short-range dI/dV spectrum. The Kondo effect [190] has also been used to prove the prominent change transfer to TCNQ and F4-TCNQ absorbed on Gr/Ru(0001) [148,188,191]. Fig. 7 shows STS measurements recorded over the TCNQ and F4-TCNQ molecules together with a STS measurement over a molecule-free Gr/Ru(0001) region. These spectra show a zero-bias peak, the signature of a Kondo resonance, over the molecules and an unstructured dI/dV curve over the clean region. From Fig. 7, we also observe that, over the center of the molecules, the Kondo resonance almost vanishes and two side resonances appear, at −42 mV and 46 mV for TCNQ and at −50 mV and 54 mV for F4-TCNQ. These peaks are due to the in-plane molecular vibration mode of the central ring of the molecules [192], which is strongly coupled to the SOMO (single occupied molecular orbital) [188]. It is also worth noticing that the absence of the Kondo resonance on the dI/dV spectra is not a signature of the absence of charge transfer. In fact, in the case of TCNQ on Gr/Ru(0001), the molecules always acquire an extra electron, due to the efficient charge transfer from the substrate to the molecule through the n-doped Graphene.[2] However, the Kondo resonance is only observed for those molecules adsorbed on the fcc sites. The mechanism behind this observation was attributed, thanks to DFT simulations, to the presence of a surface resonance in the low areas of the moiré that effectively quenches the magnetic moment for the hcp sites [191]. It is also important to remark that, despite the fact that both TCNQ and F4-TCNQ are charged upon adsorption on Gr/Ru(0001), they display a flat geometry, in contrast to the structural relaxation found for charged F4-TCNQ on Gr/Ir (111).

Finally, it is also worth mentioning that the presence of graphene may also act as a buffer layer, decoupling electronically the molecular electronic states from those of the underlying metal substrate. For example, in Ref. [193], it has been shown that it is possible to obtain high resolution images of the molecular orbitals for PTCDA, C_{60}, and pentacene adsorbed on Gr/Ru(0001). Also well resolved good molecular-orbital images have been observed for TCNQ and F4-TCNQ [148,188,191] (see Fig. 11).

5.2. Formation of 2D organic structures on graphene/metal substrates

Graphene adsorbed on metallic substrates may act as a template to induce self-assembly of organic molecules, specially those Gr/metal systems showing stronger corrugations. For example, STM measurements have shown [194] that the adsorption of pentacene molecules (see Fig. 6 (j)) on Gr/Ru(0001) occurs initially -low coverage-on the fcc sites with three possible configurations and that, only when coverage increases, hcp sites are occupied. This behavior has been rationalized, by means of DFT calculations, in terms of molecular adsorption energies, the highest one corresponding to an fcc configuration. Interestingly, the HOMO shape of the adsorbed pentacene molecules is found to be identical to the one of a free molecule, which proves the weak electronic hybridization at the pentacene-graphene interface. Also in this substrate, it is possible to induce long-range order self-assembled structures, named as loose- and close-packed structures (see Fig. 9 (a)) by

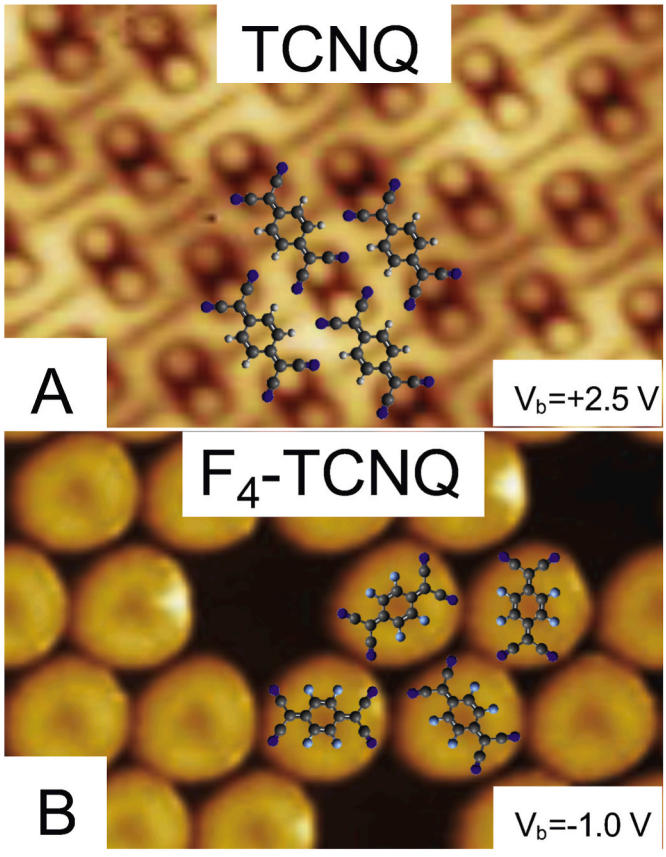

Fig. 8. (Color online) STM topographic images (5 nm × 6.25 nm, I_t = 300 pA) taken for: A) TCNQ/Gr/Ir(111) at 4.6 K; B) STM image taken for F_4-TCNQ at 77 K. Adapted from [195]. (For interpretation of the references to color in this figure legend, the reader is referred to the Web version of this article.)

[2] Here, we should point out that due to the strong chemical interaction between graphene and ruthenium the Dirac cone is not preserved but according to the calculations the graphene overlayer is n-doped. On top of the overall doping, there is a modulation in the LDOS close to the Fermi level being larger the occupied DOS in the high areas of the moiré.

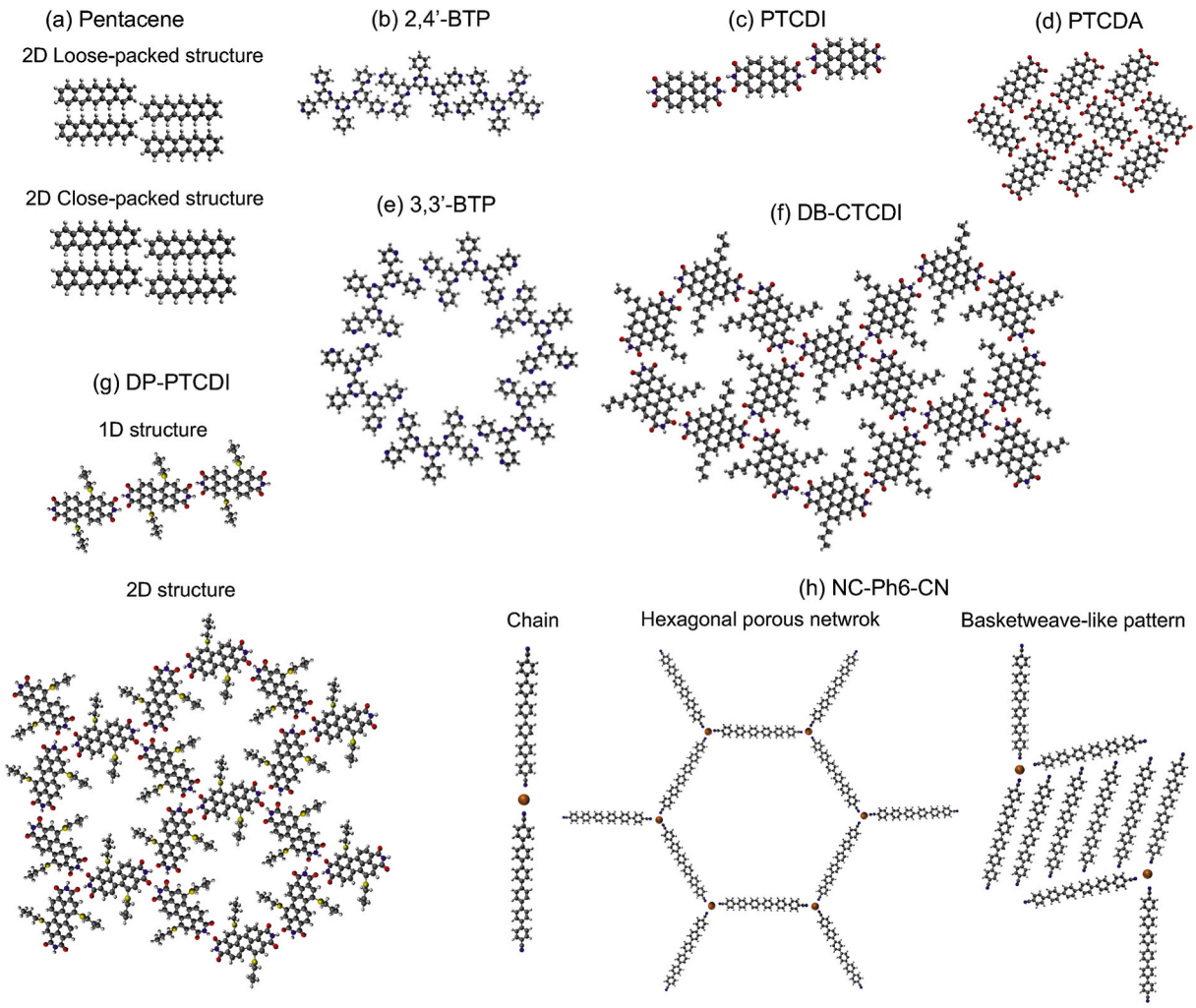

Fig. 9. (Color online) Schematic representation of the structure formed by (a) pentacene adsorbed on Gr/Ru(0001); (b) 2,4′-BTP adsorbed on Gr/Ru(0001); (c) PTCDI adsorbed on Gr/Rh(111); (d) PTCDA adsorbed on Gr/Pt(111) and Gr/Ru(0001); (e) 3,3′-BTP adsorbed on Gr/Ru(0001); (f) DB-CTCDI adsorbed on Gr/Rh (111); (g) DB-PTCDI adsorbed on Gr/Rh(111); (h) NC-Ph6-CN adsorbed on Gr/Ir(111). (For interpretation of the references to color in this figure legend, the reader is referred to the Web version of this article.)

controlling the substrate temperature and the deposition rate [194].

The formation of two-dimensional (2D) organic molecular structures on Gr/metal substrates is the result of the competition between the intermolecular interaction and the molecule-surface interaction. Depending on the result of such competition, a bunch of organic molecules may form 2D structures or remain isolated. An illustrative example of this phenomenon is the adsorption of TCNQ and F4-TCNQ on Gr/Ru (0001) (see Fig. 8). Whereas the former molecules form densely packed linear magnetic arrays and even a complete monolayer (see section 5.3.1 for details), the latter ones remain as isolated magnets [148]. This behavior was understood from a detailed analysis of the two mentioned interactions. DFT calculations showed, on the one hand, that both TCNQ and F4-TCNQ share similar charge transfer and magnetic properties and, on the other hand, that the intermolecular delocalization of the transferred electron is fundamental to determine the self-assembly of the molecules. In the case of TCNQ, as a result of the favorable overlap between the clouds of neighboring molecules, electron delocalization stabilizes the charged TCNQ aggregates on the surface. On the contrary, for F4-TCNQ, the much less favorable overlap inhibits an effective electron delocalization, what makes intermolecular repulsion to prevail [148]. In the case of the Gr/Ir(111) substrate, it has also been observed, using STM measurements, a significant difference between adsorbed TCNQ and F4-TCNQ. Whereas the former molecules form a well-ordered self-assembled monolayer induced by the attractive electrostatic interaction between the excess of negative charge in the cyano groups and the excess of positive charges in the hydrogen atoms of the central rings, the latter form a fairly regular hexagonal array of rotating molecules adsorbed at the hcp sites (see Fig. 8 B). This behavior of F4-TCNQ molecules has been attributed to the negative electrostatic potential created by the four fluorine atoms around the central ring, which hinders the self-assembly based on attractive interaction between molecules [195]. At this point, it is worth noticing that, although TCNQ forms complete compact monolayers on both Gr/Ru(0001) and Gr/Ir(111), the electronic characteristics of these monolayers are rather different [196]. X-ray photoemission measurements have revealed the absence of charge transfer to TCNQ molecules adsorbed on Gr/Ir(111) and the site-dependent charge transfer to TCNQ adsorbed on Gr/Ru(0001), in such a way that molecules adsorbed on the low areas of the moiré are charged and develop a magnetic moment as evidenced by the presence of the corresponding Kondo resonance in the STS spectrum, whereas those molecules absorbed on the high areas of the moiré remain neutral. This phenomenon accounts for the spatially dependent long-range magnetic order observed for TCNQ/Gr/Ru(0001) [197] that it is explained in detail in sec. 5.3.1.

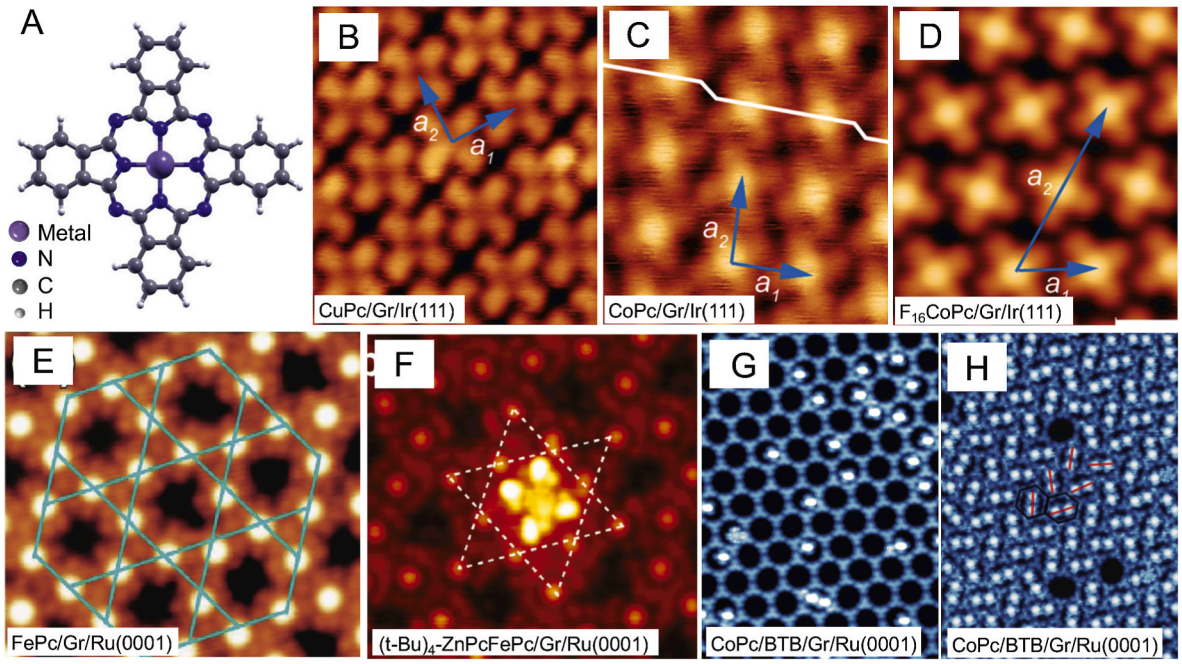

Fig. 10. (Color online) (A) General geometry of a metal-phthalocyanine molecule; (B), (C) and (D) Fast Fourier transform (FFT) image of a CuPc, a CoPc and a F_{16}CoPc monolayer adsorbed on Gr/Ir(111), respectively, (adapted with permission from Ref. [205]); (D) STM images obtained for FePC adsorbed on Gr/Ru(0001), the blue lines mark the unit cell of the Kagome lattice (adapted with permission from Ref. [206]); (F) STM image of single-guest (*t*-Bu)$_4$- ZnPc molecules hosted by a FePc Kagome lattice on Gr/Ru(0001) (adapted with permission from Ref. [207]); (G) and (H) STM images of low and high coverage CoPc molecules, respectively, in a BTB molecule network adsorbed on Gr/Ir(111) (adapted with permission from Ref. [208]). (For interpretation of the references to color in this figure legend, the reader is referred to the Web version of this article.)

Moiré structures induced in graphene adsorbed on metal substrates have also shown their ability to rule the self-organization of other complex organic molecules. For example, perylene tetracarboxylic diimide (PTCDI) forms pairs of parallel long one-molecule-width rows following the high-symmetry directions of the Gr/Rh(111) surface (see Fig. 9 (c)) [198]. This is in contrast with the case of graphite substrates, where PTCDI forms 3D islands. The molecular rows obtained in the Gr/Rh case grow in a commensurate way thanks to the match between the molecule-molecule spacing and the lattice parameter of the graphene superstructure. If PTCDI is replaced by its derivate 1,7-dipropylthio-perylene-3,4:9,10-tetracarboxydiimide (DP-PTCDI) -see Fig. 6 (f)- the formation of commensurate rows is also observed (see Fig. 9 (g)), but in this case row pairs are uncommon. These DP-PTCDI molecules form more commonly three-molecule junctions (see Fig. 9 (g)) [198]. In the case of 1,7-di(butyl)-coronene-3,4:9,10-tetracarboxylic acid bisimide (DB-CTCDI) -see Fig. 6 (g)-, three-molecule junctions also dominate and a honeycomb monolayer structure (see Fig. 9 (f)) is formed on the surface. Binding energies computed at DFT theory level revealed that trimers are more stable than dimers for these three molecules PTCDI, DP-PTCDI, and DB-CTCDI in gas phase, however the strain suffered by the trimer junctions on the Gr/Rh(111) surface reduced their binding energies favoring the formation of dimers, except for DB-CTCDI, the molecule with the strongest trimer junction [198]. The self-assembly of a similar molecule, PTCDA on Gr/Pt(111) shows a completely different behavior, as revealed by STM and STS measurements and DFT calculations [199]. PTCDA molecules form a herringbone pattern (see Fig. 9 (d)) on Gr/Pt(111). In this system, the weak coupling between graphene and Pt(111) induces a weak coupling between PTCDA and the substrate, i.e., the electronic features of the molecular monolayer remain unaltered upon adsorption on Gr/Rh(111). A 2D herringbone pattern has also been observed (STM images) for PTCDA adsorbed on Gr/Ru(0001) [200], despite the strong corrugation of graphene on Ru(0001). This behavior of PTCDA on Gr/Ru(0001) has been attributed, based on DFT calculations, to the strong intermolecular interactions ruled by C–H···O type hydrogen bonds, which overcompensate the lateral corrugation of the adsorption potential. The intermolecular interaction (C–H···N type hydrogen bonds), on the other hand, is not enough to compensate the lateral corrugation of the adsorption potential for 2-phenyl-4,6-bis-(6-(-pyridin-3-yl)-4-((pyridin-3-yl)pyridin-2-yl)pyrimidine (3,3′-BTP). As a result, 3,3′-BTP molecules occupy preferably the valley regions forming linear or ring-like (see Fig. 9 (e)) structures [200]. The inner diameter of these ring-like structures is large enough to host additional molecules, and it has been found that host 3,3′-BTP molecules may rotate freely inside the rings. A similar behavior has been observed for self-assembly of 2,4′-bis(terpyridine) (2,4′-BTP) [201] on Gr/Ru(0001). The high corrugation in the adsorption potential induces the preferential adsorption on the valley region, and the subsequent formation of 1D molecular chains. Formation of 1D chains (see Fig. 9 (h)), 2D basketweave-like patterns and hexagonal porous networks (see Fig. 9 (h)) mediated by Cu atoms coadsorption has been observed, by means of STM, for para-hexaphenyl-dicarbonitrile (NC-Ph_6-CN) -see Fig. 6 (l)- on Gr/Ir(111) [202]. Furthermore, as proven by STS measurements, for this system the type of bonding configuration determines the electronic properties of the adsorbates [202]. On clean Gr/Cu(111) absorbed NC-Ph_6-CN molecules self-assemble forming a close-packed structure consisting of rows of parallel molecules showing a shift along the molecular axis for every fourth or fifth molecule along a row [203]. 1,3,5-benzenetribenzoic acid (BTB) -see Fig. 6 (k)- also forms hexagonal porous networks on Gr/Cu(111) [204]. This pattern is the result of the double hydrogen bonding between the carboxylic acid end groups of the BTB molecules. In this case, the presence of the graphene layer prevents the deprotonation of BTB, which commonly occurs upon adsorption of BTB on Cu(111), but the metallic substrate still influences the organization of the BTB molecules, because these are aligned according to the graphene lattice that aligns itself along the principal directions of Cu (111).

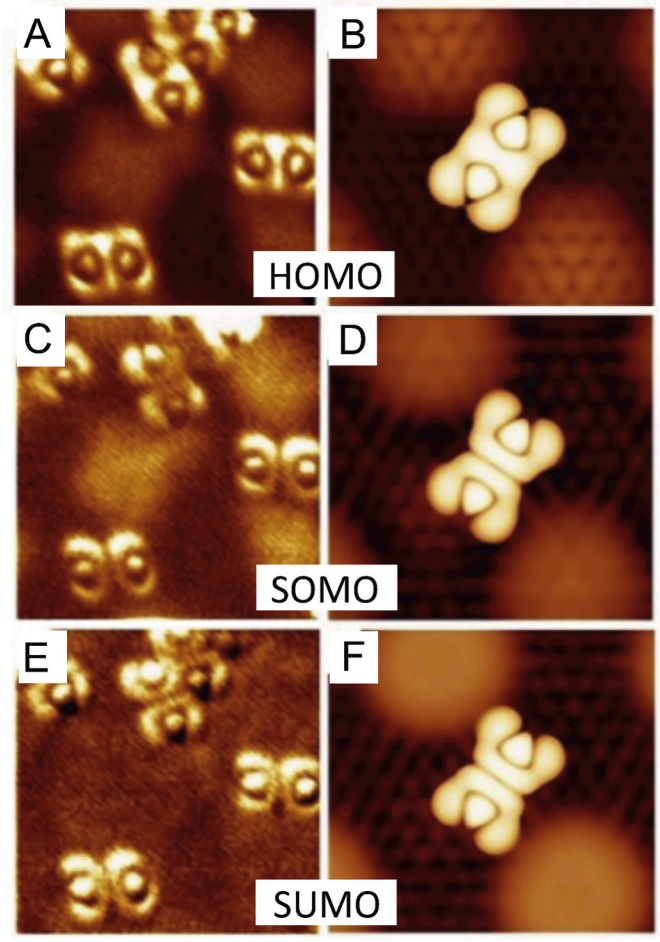

Fig. 11. (Color online) Experimental (left column) and theoretical (right column) STM images showing the frontier molecular orbitals of TCNQ adsorbed on Gr/Ru(0001). (A) and (B) $V_b = -2.0$ V; (C) and (D) $V_b = -0.8$ V; (E) and (F) $V_b = +1.0$ V. Adapted from [197]. (For interpretation of the references to color in this figure legend, the reader is referred to the Web version of this article.)

Another relevant family of organic molecules that are able to self-assemble in Gr/metal substrates is the phthalocyanines family (see Fig. 10 A). H_2Pc, NiPc, FePc, and MnPc, for example, are able to form Kagome lattices[3] when adsorbed on Gr/Ru(0001) [206,210]. Thanks to the versatility of the Pc molecules, the molecular spin can be altered just by varying the central atom, making 2D Pc structures ideal models for studying spin frustration and also to be exploited for spintronic applications. In these examples, the role of Gr/Ru(0001) substrates is twofold: (i) graphene acts as a buffer layer decoupling the Pc molecules from the metal substrate preserving their intrinsic electronic properties; (ii) Pc molecules occupy the hcp and fcc sites leaving the atop site entirely empty, i.e., the Pc network follows the periodicity of the moiré pattern. This site-dependent adsorption has been rationalized in terms of lateral electric dipoles originated from the inhomogeneous charge distribution in the graphene monolayer induced by the epitaxial constraint of graphene on Ru(0001) [211]. The FePc/Gr/Ru(0001) Kagome lattice (see Fig. 10 E) has been shown to be an ideal scaffold for host-guest superstructures. STM measurements [207] have shown that FePc and *tert*-butyl ZnPc co-adsorbed on a FePc Kagome lattice occupy preferentially the nanoscale pores of the lattice (see Fig. 10 F) forming ordered superstructures with alternate rows of FePc and *tert*-butyl ZnPc, and that the formation of this superstructure is ruled by the long-range interaction between the two guest molecules mediated by the Kagome lattice. If another metal substrate is considered, the Pc 2D network can present a completely different geometry. For example, FePc molecules adsorbed on Gr/Pt(111) display a square lattice shape, regardless the moiré pattern exhibited by the various Gr/Pt(111) domains present in the substrate [210]. The molecule-substrate interaction in this latter case is weaker than for FePc on Gr/Ru(0001). Also weak is the interaction of FePc with the Gr/Ir(111) substrate [212]. On this substrate, the FePc molecules form a planar flat-laying array and graphene acts just as buffer layer decoupling the molecule from the metal. This preserves their basic intrinsic molecular properties, but at the same time confers new properties to the system, such as an enhancement of the magnetic anisotropy, as deduced from X-ray magnetic circular dichroism measurements [213], or the slight n-doping of graphene, as revealed by core-level photoemission and absorption spectroscopy measurements [214]. On Gr/Ni(111), it has been shown by means of AFM and HREELS [215] that FePc molecules group into 1D fiber-like islands due to the comparable intermolecular and molecule-substrate interactions, and that the orientation of these 1D islands is determined by the coupling between graphene and Ni(111). Similar experiments have revealed that CuPc, on the contrary, nucleate in 2D islands, because in this case the intermolecular interaction widely dominate over the molecule-substrate one [215]. On Gr/Ir(111), the intermolecular interaction also rules the formation of a planar-2D CuPc square lattice (see Fig. 10 B) [205]. However, on this same substrate, CoPc molecules, albeit also forming an ordered square lattice [216], interact more strongly with the substrate, which leads to the appearance of kinks along one of the CoPc square lattice directions (see Fig. 10C). This does not mean that the intermolecular interaction is negligible. In fact, when the peripheral hydrogens of CoPc are substituted by fluorine atoms, the CoPc square lattice formed on Gr/Ir(111) becomes an oblique lattice (see Fig. 10 D). The different self-assembly of these three Pc's, CuPc, CoPc, and F_{16}CoPc, has been rationalized, based on DFT calculations, in terms of the energies and symmetries of the frontier molecular orbitals [205]. On Gr/Ru(0001), on the other hand, the CoPc molecules form an ordered Kagome lattice [217] similar to the lattice formed FePc molecules [206,210]. The growth of 2D CoPc structures can be controlled using organic open superstructures previously adsorbed in the substrate, as scaffolds. This is the case for the adsorption (see Fig. 10 G) and self-assembly (see Fig. 10H) of CoPc on the flexible nanopores network created upon adsorption of 1,3,5-benzenetribenzoic acid (BTB) on Gr/Ir(111) [208]. As shown by Banerjee et al. [208], these flexible BTB scaffolds can be used, for example, to form CoPc dimer structures.

Finally, it is also worth mentioning the formation of 2D fullerene structures. In 2012 a combined STM and DFT study [218] showed that fullerene molecules assemble on Gr/Ru(0001) forming a perfect periodic hexagonal supramolecular structure disregarding the underlaying corrugation, disorder or steps, which was explained in terms of the weak interaction between the C_{60} molecules and the substrate. However, this interaction is not negligible at all, as proven in Ref. [219], where it was shown that the moiré structure presents a singular diffusion barrier that limits the mobility of the C_{60} on the surface, thus influencing the way the molecule monolayer grows. At low coverage, the fullerenes adsorb on the hcp valley regions, where they are free to rotate. Once these sites are populated, the molecules adsorb on the fcc valley regions, subsequently on the top regions, and finally on the remaining moiré sites. When the coverage increases, the C_{60}–C_{60} interaction induces the freezing of the molecular rotations. As stated in Ref. [219], if one replaces bare fullerenes by endohedral fullerenes with magnetic spins, these rotationally frozen molecular structures can be useful for applications in molecular spintronics. On the other hand, C_{60} molecules self-assemble on Gr/Cu (111), forming a (4 × 4) superstructure, without any influence of the

[3] A 2D pattern showing geometrically frustrated magnetic properties composed of interlaced triangles in such a way that each lattice point have four neighbors [209].

underlying moiré pattern [220].

5.3. Organic molecule/Gr/Ru(0001) systems: A few singular examples

5.3.1. Long-range magnetic properties of TCNQ on Gr/Ru(0001)

The peculiar characteristics of rippled graphene lying on a Ru(0001) substrate, in particular, the n-doping of the carbon monolayer [129,173,221,222], has been exploited to selectively induce charge transfer from this substrate to electron acceptor molecules, in particular, TCNQ, and to build organic 2D arrays with long-range magnetic order [148,191,197]. This is possible because, as discussed above, graphene prevents the formation of TCNQ-Ru(0001) bonds while allowing for efficient charge transfer from the Gr/Ru(0001) substrate to the molecules. Since the transferred charge extends over intermolecular bands with well-defined spin character, it has been proposed that TCNQ monolayer could be used to add magnetic functionalities to graphene (e.g., by altering the spin polarization of a current flowing through it).

In the experiment reported in Ref. [197], TCNQ molecules were deposited on Gr/Ru(0001) at 300 K and imaged with STM at 4.6 K. At low coverage, TCNQ molecules always adsorb at the lower parts of the moiré and the topographic STM images exhibit intramolecular resolution at different bias voltages (see Fig. 11). Such a resolution is not seen when TCNQ is directly deposited on metal surfaces. DFT calculations reported in the same work show that the TCNQ-graphene distance is about 3 Å, which suggests a weak molecule-graphene coupling. Nevertheless, thanks to its n-doping, graphene is still able to transfer a fraction of electron to the LUMO of the neutral molecule, thus leading to a splitting into a Single Occupied Molecular Orbital (SOMO) and a Single Unoccupied Molecular Orbital (SUMO). As can be seen from Fig. 11, the SOMO and SUMO exhibit the characteristic central node of the original LUMO, whereas the HOMO does not. The observed features are in excellent agreement with those obtained from DFT calculations (see Fig. 11 bottom panels). These calculations show that, as a consequence of the different partial filling of the SOMO and SUMO, the adsorbed TCNQ molecule develops a magnetic moment of approximately 0.4 μB. This reflects in a prominent Kondo peak, which has been observed experimentally and thoroughly analyzed in Ref. [148]. A similar magnetization has been observed in isolated F4-TCNQ molecules lying of Gr/Ru(0001) [148].

When 1 ML TCNQ coverage is achieved by forcing the molecules to also occupy the upper parts of the ripples, the images recorded at the SOMO (−0.8 V) -Fig. 12 C- and SUMO (+1.0 V) -Fig. 12 E−energies reveal the presence of tube-like structures separated by clear nodes, indicating that TCNQ intermolecular states are formed over the whole

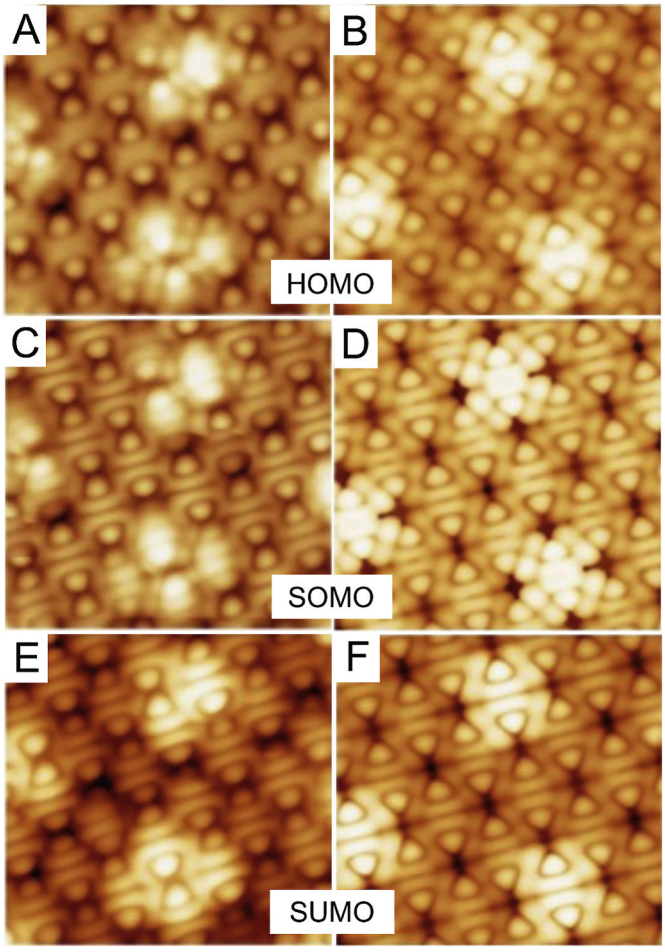

Fig. 12. (Color online) Experimental (left column) and theoretical (right column) STM images showing intermolecular band formation in 1 ML TCNQ adsorbed on Gr/Ru(0001). (A) and (B) $V_b = -2.0$ V; (C) and (D) $V_b = -0.8$ V; (E) and (F) $V_b = +1.0$ V. Adapted from [197]. (For interpretation of the references to color in this figure legend, the reader is referred to the Web version of this article.)

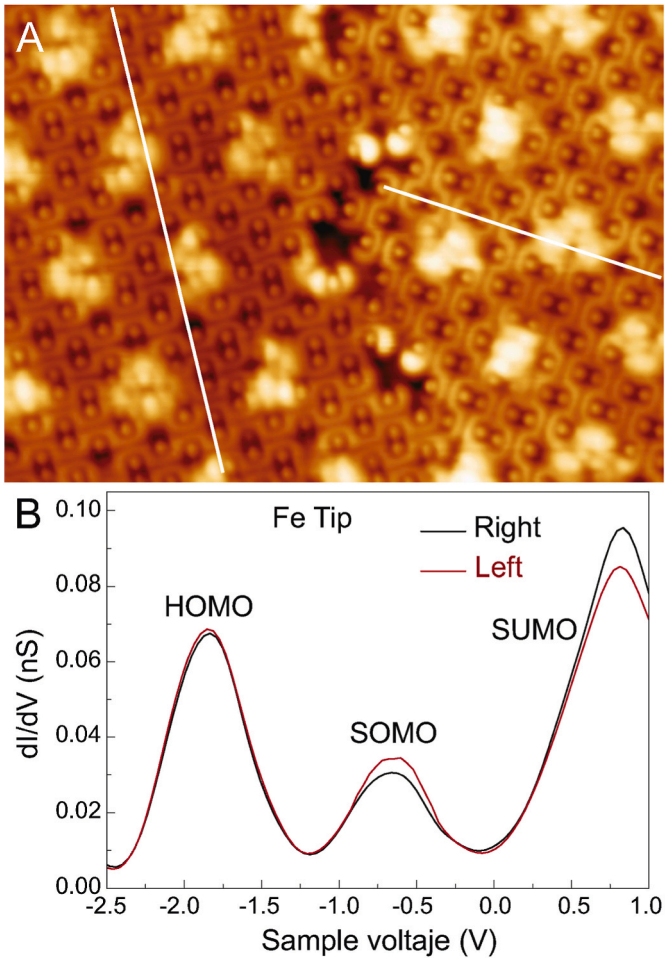

Fig. 13. (Color online) (A) Spin polarized STM measurements (16.7 nm × 12.1 nm) recorded at $V_b = +1.5$ V and $I_t = 100$ pA; (B) spin-resolved differential tunelling conductance averaged over three moiré unit cells in each domain. Adapted from [197]. (For interpretation of the references to color in this figure legend, the reader is referred to the Web version of this article.)

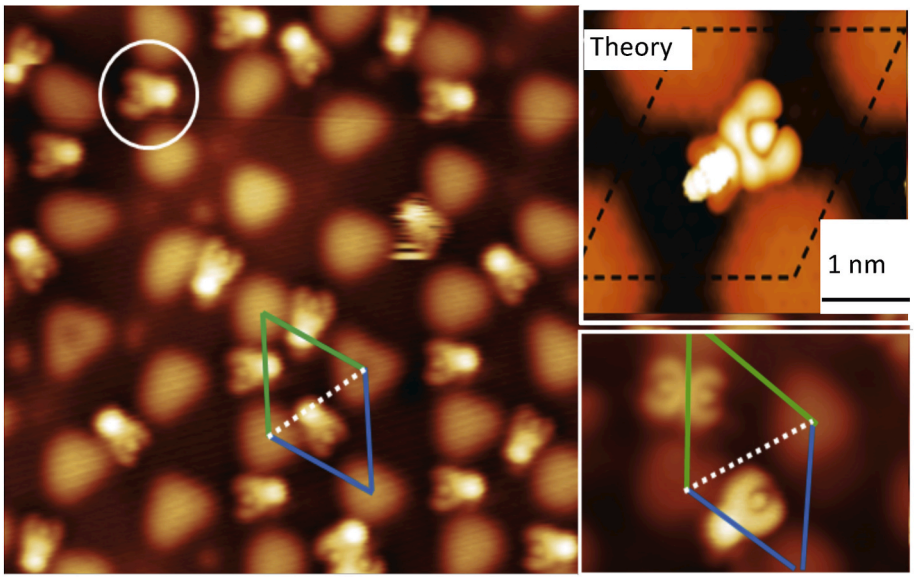

Fig. 14. (Color online) STM topographic image (27 nm × 15 nm, $V_b = -1.5$ V, $I_t = 5$ pA) of CH_2CN and TCNQ deposited on G/Ru(0001) after the reaction at room temperature. The lower inset is a blow up of a single molecule and the upper inset the calculated STM image. Adapted from Ref. [137]. (For interpretation of the references to color in this figure legend, the reader is referred to the Web version of this article.)

surface. These features are similar to those predicted by theory (Fig. 12 D and F), which further shows that, in this case, the average magnetic moment per molecule is 0.18 μB. Detailed Spin Polarized STM measurements over two TCNQ domains (i.e., with different orientation with respect to the graphene lattice) revealed the existence of magnetic contrast due to long range magnetic order in the TCNQ adlayer at 4.6 K (see Fig. 13 A), thus confirming the above predictions. Indeed, as Fig. 13 B shows, the spin-resolved differential tunneling conductance averaged over three moiré unit cells associated with two different domains are different. As expected, the spectrum exhibits pronounced HOMO (−1.8eV), SOMO (−0.75 eV) and SUMO (+0.75 eV) peaks, but the relative intensity of the SOMO and SUMO peaks is inverted between domains. In contrast, the spectra are nearly identical in the two domains at the HOMO peak, since the HOMO is filled by two electrons and, therefore, cannot exhibit any magnetic property. A similar long range magnetic order is not observed in F4-TCNQ deposited on Gr/Ru(0001), since, as discussed in previous sections, electron delocalization between neighboring molecules is not possible due to the presence of the F atoms.

5.3.2. *Reversible formation of C–C bonds on Gr/Ru(0001)*

Pure carbon is known to be a catalyst poison. However, it has been shown [137] that Gr/Ru(0001) can promote chemical reactions that would hardly take place without the assistance of a catalyst. Indeed, epitaxial graphene grown on Ru(0001) can promote the reversible formation of a C–C bond between cyanomethylene groups (-CH_2CN), covalently bonded to the graphene surface at specific positions, and TCNQ, which as explained in the previous section, is physisorbed on graphene and, therefore, can diffuse.

Fig. 14 shows STM images measured at 4.8 K after deposition of TCNQ on Gr/Ru previously patterned with cyanomethylene groups. Most TCNQ molecules look very different from those deposited in the absence of –CH_2CN (see Fig. 14). One half of the TCNQ molecule remains practically unperturbed, showing the same intramolecular resolution as pristine TCNQ, while the other half appears as a bright protrusion with no internal resolution. No individual cyanomethylene substituents are observed in the graphene surface, although they were covalently bonded to graphene (hence, visible in STM images) before addition of TCNQ. Also, all molecules are adsorbed on the bridge areas

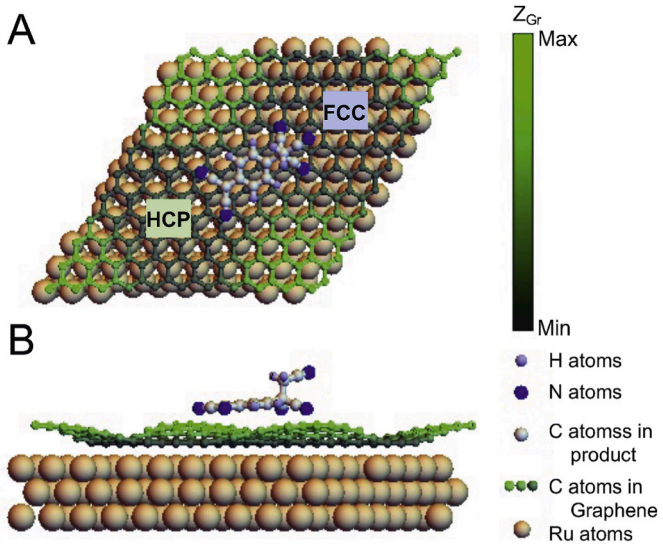

Fig. 15. (Color online) (A) Top view of the most stable adsorption configuration on Gr/Ru(0001). The molecule is adsorbed on the bridge position with the cyanomethylene end pointing towards the FCC- Top areas of the moiré pattern. (B) Lateral view of the most stable configuration. The cyanomethylene group is located on top of the TCNQ and points towards the vacuum. Adapted from Ref. [137]. (For interpretation of the references to color in this figure legend, the reader is referred to the Web version of this article.)

with the bright protrusion pointing to the FCC areas.DFT calculations that explicitly include the ruthenium substrate, the rippled graphene monolayer and TCNQ-CH_2CN molecules, where a C–C bond has been formed between TCNQ and –CH_2CN, lead to STM images in excellent agreement with the experimental ones, thus showing that the C–C bond is actually formed. The disposition of the molecule on the Gr/Ru surface predicted by these calculations is shown in Fig. 15.

The catalytic role of graphene in this particular reaction is the consequence of three effects. First, graphene allows for an efficient

charge transfer from Ru(0001) to both reactants, thus allowing for changes in the carbon hybridization. Second, graphene holds the $–CH_2CN$ groups in fixed positions and allows the reduced TCNQ molecules to diffuse on the surface. Finally, it prevents TCNQ molecules from reacting with the Ru(0001) surface. It is only the concerted action of these three effects that allows for the formation of the TCNQ-CH_2CN complex. At variance with TCNQ molecules adsorbed in Gr/Ru(0001), this complex does not present a magnetic moment, therefore, it does not present Kondo resonances.

A very interesting observation reported in Ref. [137] is that the reaction is fully reversible by injection of electrons from the STM tip at voltages >+1.7 eV. At this voltage, electrons are injected in the LUMO of the TCNQ-CH_2CN complex, which due to its antibonding character, leads to the breakup of the C–C bond and the recovery of physisorbed TCNQ and CH_2CN- bonded to graphene. The making and breaking of this bond is accompanied by the switching off and on of a Kondo resonance, so that the system can be viewed as a reversible magnetic switch controlled by a chemical reaction.

5.3.3. *Nonacenes photogeneration*

Graphene/Ru(0001) has been recently proposed for efficient on-surface photogeneration of large acenes from α-bisdiketone precursors. This is a relevant problem since acenes longer than pentacene have low solubility and are highly reactive, which has prevented their synthesis in solution. As discussed in section 4.2, Gr/Ru(0001) has an unoccupied electronic state at +2.85 eV above the Fermi level, which originates from the mixture of a Ru(0001) surface resonance and a graphene image state. Reaching this empty state requires approximately the same energy as that of the n-π^* transition of the diketone group, which makes it ideal to promote electron transfer from a photoexcited α-bisdiketone, hence to undergo a chemical reaction. In a recent work reported in Ref. [223], α-bisdiketone molecules were deposited on Gr/Ru and exposed to visible light of 470 nm for 90 min, leading to the conversion of all precursors into nonacenes (100% efficiency).

Fig. 16 A shows a submonolayer coverage of α-bisdiketone nonacene precursors resulting from sublimation under dark conditions at room temperature. The inset shows a topographic STM image of one of these precursors, exhibiting two bright protrusions of similar apparent height, which are associated with the bridged α-diketone groups pointing upwards. After irradiation of the sample by visible light of 470 nm for 90 min, photodecarbonylation of α-bisdiketone nonacene takes place, leading to the formation of nonacenes. Fig. 16B shows an STM image of one of the formed nonacenes, which at variance with that of α-bisdiketone shown in the inset of Fig. 16 A, is uniform in apparent height. The DFT simulated STM image shown on the right of Fig. 16 B confirms that the observed image corresponds to nonacene physisorbed on Gr/Ru (0001) and that the observed intramolecular structure resembles that of the nonacene LUMO in the gas phase. The reaction takes place because both the α-bisdiketone nonacene precursors and the above-mentioned surface image state are localized in the low areas of the moiré.

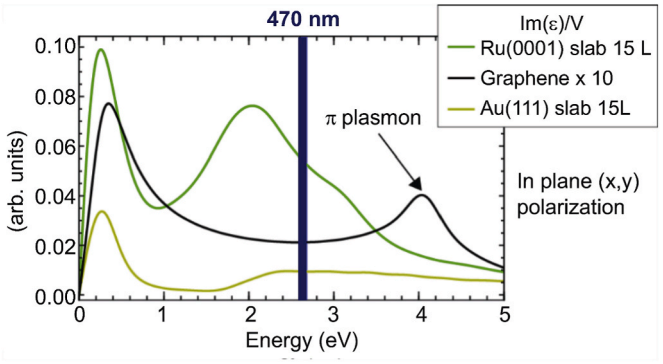

Fig. 17. (Color online) Absorption spectra per unit volume of Ru(0001), Au (111) and pristine graphene obtained in a Linear Response TD-DFT calculation. The graphene results are multiplied by 10. The vertical blue line marks the energy position of the light used in the experiments. Adapted from Ref. [223]. (For interpretation of the references to color in this figure legend, the reader is referred to the Web version of this article.)

It is important to stress that the reported efficiency represents a gain of more than a factor of two with respect to the similar process occurring on a Au(111) substrate [224]. This requires that the Gr/Ru(0001) substrate efficiently absorbs photons in order to significantly populate the surface states with hot electrons. The absorption spectrum per unit volume shown in Fig. 17 confirms that this is indeed the case. The intensity of the spectrum around 470 nm is more than twice larger for Ru (0001) than for Au(111). This is due to the presence of empty d bands just above the Fermi level, which is not the case for Au. The spectrum of Gr/Ru(0001) is also more than an order of magnitude more intense than that of pristine graphene. Therefore, the observed high photogeneration yield on Gr/Ru(0001) results from the combination of (i) the high photon absorption on Ru(0001) and (ii) the appearance of a spatially localized surface state at the right energy due to the presence of the graphene adlayer.

6. Concluding remarks and outlook

Throughout this manuscript, we have reviewed our current understanding of the properties of graphene adsorbed on metal surfaces and its use as a template for adsorption and arrangement of organic molecules. Upon generation on a metal substrate, graphene may remain adsorbed pseudomorphically, when the lattice parameters of both periodic structures are comparable, or may suffer a strong distortion

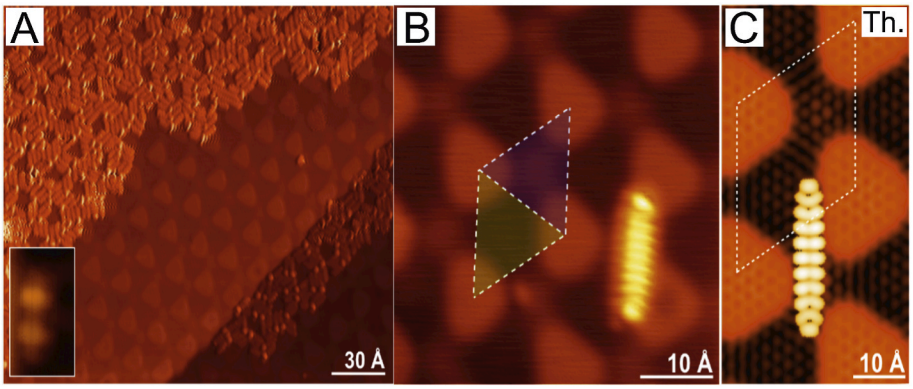

Fig. 16. (Color online) (A) STM topography (Vb = 1.5 V, It = 50 pA) image of α-bisdiketone nonacene precursors on Gr/Ru(0001) after room temperature deposition, recorded at 4.6 K. Inset shows a topographic image of a single α-bisdiketone nonacene precursor. (B) STM image (Vb = 1.7 V, It = 100 pA) of a nonacene molecule adsorbed on the Gr/Ru(0001) surface after being exposed to visible light (λ = 470 nm) for 90 min. (C) simulated STM image. Adapted from Ref. [223]. (For interpretation of the references to color in this figure legend, the reader is referred to the Web version of this article.)

leading to the formation of a moiré. Similarly, when the interaction between graphene and the metal is weak (physisorption), the graphene electronic properties may remain almost unaltered, but when the interaction is strong (chemisorption), graphene can be n-doped, due to electron transfer from the metal to graphene, or p-doped, due to electron transfer from graphene to the metal. This variety of scenarios make graphene/metal substrates ideal templates to adsorb organic molecules under very different conditions. For example, flat physisorbed graphene can act as a buffer layer that keeps the adsorbed molecules isolated from each other and decoupled from the metal surface, which allows one, among other things, to perform detailed studies of the electronic and structural properties of these molecules, not possible in the gas or the condensed phases. But the deposited molecules can also experience the transfer of electrons from and to graphene, which may eventually lead to the formation of magnetic structures, or even lead to the formation of organic monolayers. Also, the chemisorbed graphene, thanks to its moiré pattern, can boost the formation of 1D and 2D organic structures with functionalities as a result of the competition between the graphene-molecule and the molecule-molecule interactions.

From all the possible graphene/metal templates, Graphene/Ru (0001) is the one that has received the most attention and the one that has been revealed as the most versatile to date due to its exceptionally large corrugation and the strong n-doping of the lower areas of its moiré. Among organic molecules, the phthalocyanines family has been the most widely studied, although other organic molecules, from small ones as TCNQ and TTF to large polymeric compounds, have been successfully uses.

We are still far away from having exploited the full potentiality of graphene/metal substrates. Apart from the obvious possibility of exploring other families of organic molecules and other single-metal substrates, it would be interesting to consider the case of bimetallic substrates to improve on the tunability of the electronic properties of graphene and its moiré. Both alloys and monolayers of metals grown on different metal substrates could contribute to achieve this goal, as well as intercalation of alkali or transition-metal atoms in between the graphene layer and the metal substrate. There are neighboring research fields that could also benefit very much from this systems, as, e.g., the field of single-molecule junctions. Indeed, the modulation of the electronic properties of graphene all over the moiré could be used to modulate the conductivity in these molecular junctions depending on the specific anchoring site on the graphene/metal electrode. Also, the high elasticity of the high areas of the moiré, which exhibit elastic constants as high as 40 N/m in graphene/Ru substrates [222], could be used to build very flexible organic superstructures. And what about the existence of localized electron pockets in those same high areas? They constitute a network of quantum dots that, by choosing the appropriate organic molecules, could lead to periodic structures of interacting quantum dots interconnected by the molecules that occupy the lower areas of the moiré. Certainly, the deposition of organic molecules on graphene/metal substrates will continue to provide us with new unexpected findings and some surprises in the coming years.

All the knowledge acquired for Gr/metal systems will also be valuable for the development of new templates involving other two-dimensional materials adsorbed on transition metal surfaces. In this respect, boron nitride (h-BN) on Rh(111), that forms a moiré structure of combined wires and nanopores, has already been used as a template for the adsorption of C60 molecules [225], showing the existence of a phase transition between randomly oriented molecules at room temperature and ordered molecules with a common orientation at low temperature [226]. This same template has also been employed to adsorb F4-TCNQ [227] and azobenzene molecules, h-BN/Cu(110) to create herringbone structures of PTCDA molecules, and b-BN/Cu(111) [228,229] and h-BN/Ir(111) [230] to adsorb a variety of other organic molecules. 2D metal diselenides have also been grown on transition metals. For example, PtSe2 (CuSe) grown on Pt (Cu) substrates form triangular patterns where organic molecules, such as Pentane (FePc), can get adsorbed and form ordered structures [231]. No doubt, the exclusive properties of these non-graphene-based templates, in combination with those already reported and the ones to come for graphene-based substrates, will widen the range of applicability and control of molecular adsorption in 2D materials grown in metal substrates.

Declaration of competing interest

The authors declare that they have no known competing financial interests or personal relationships that could have appeared to influence the work reported in this paper.

Acknowledgements

This work has been supported by the MICINN projects PID2019-105458RB-I00, PID2019-106732GB-I00 and PGC2018-093291-B-I00. 'Severo Ochoa' Programme for Center of Excelence in R&D (CEX2020-001039-S) and 'María de Maeztu' Programme for Units of Excellence in R&D (CEX2018-000805-M).

List of acronyms

AES Auger electron spectroscopy
AFM atomic force miscroscopy
ARPES Angle-resolved photoemission spectroscopy
BTB 1,3,5-benzenetribenzoic acid
CVD Chemical vapor deposition
DDQ 2,3-dichloro-1,4-benzoquinone
DB-CTCDI 1,7-di(butyl)-coronene-3,4:9,10-tetracarboxylic acid bisimide
DP-PTCDI 1,7-dipropylthio-perylene-3,4:9,10-tetracarboxydiimide
DFT Density functional theory
FER Field emission resonance
F4-TCNQ tetrafluoruro-tetrocyanoquinodimethane
GGA Generalized gradient approximation
HREELS High-resolution electron energy loss spectroscopy
LDA Local density approximation
LEED Low-energy electron diffraction
MO Molecular orbital
NC-Ph$_6$-CN *Para*-hexaphenyl-dicarbonitrile
Pc Phthalocyanine
PTCDA Perylene-3,4,9,10-tetracarboxylic-3,4,9,19-dianhidride
PTCDI Perylene-3,4,9,19-tetracarboxylic-3,4,9,10-dianhydride-diimide
RHEED High-energy electron diffraction
STM Scanning tunneling microscopy
STS Scanning tunneling spectroscopy
TDS Thermal desorption spectroscopy
TCNQ Tetracyanoquinodimethane
TCNE Tetrocyanoethylene
TIF Tetrathiofulvalene
UHV Ultra high vacuum
UPS Ultraviolet photoelectron spectroscopy
vdW van der Waals
XPD X-ray photoelectron diffraction
XPS X-ray photoelectron spectroscopy
4-amino-TEMPO 4-amino-2,2,6,6,-tetramethyl-1-piperridinyloxy
2,4′-BTP 2,4′-bis(terpyridine)
3,3′-BTP 2-phenyl-4,6-bis-(6-pyridin-3-yl)-4-((oyridin-3-yl)pyridin-2-yl)pyrimidine

References

[1] K.S. Novoselov, A.K. Geim, S.V. Morozov, D. Jiang, Y. Zhang, S.V. Dubonos, I. V. Grigorieva, A.A. Firsov, Electric field effect in atomically thin carbon films, Science 306 (2004) 666–669, https://doi.org/10.1126/science.1102896.

[2] J.W. May, Platinum surface LEED rings, Surf. Sci. 17 (1969) 267–270, https://doi.org/10.1016/0039-6028(69)90227-1.
[3] J. Grant, T. Haas, A study of ru(0001) and rh(111) surfaces using LEED and auger electron spectroscopy, Surf. Sci. 21 (1970) 76–85, https://doi.org/10.1016/0039-6028(70)90064-6.
[4] C. Oshima, A. Nagashima, Ultra-thin epitaxial films of graphite and hexagonal boron nitride on solid surfaces, J. Phys. Condens. Matter 9 (1997) 1–20, https://doi.org/10.1088/0953-8984/9/1/004.
[5] J. Shelton, H. Patil, J. Blakely, Equilibrium segregation of carbon to a nickel (111) surface: a surface phase transition, Surf. Sci. 43 (1974) 493–520, https://doi.org/10.1016/0039-6028(74)90272-6.
[6] L. Isett, J. Blakely, Segregation isosteres for carbon at the (100) surface of nickel, Surf. Sci. 58 (1976) 397–414, https://doi.org/10.1016/0039-6028(76)90478-7.
[7] M. Eizenberg, J. Blakely, Carbon monolayer phase condensation on ni(111), Surf. Sci. 82 (1979) 228–236, https://doi.org/10.1016/0039-6028(79)90330-3.
[8] B. Lang, A leed study of the deposition of carbon on platinum crystal surfaces, Surf. Sci. 53 (1975) 317–329, https://doi.org/10.1016/0039-6028(75)90132-6.
[9] J.C. Hamilton, J.M. Blakely, Carbon layer formation on the pt (111) surface as a function of temperature, J. Vac. Sci. Technol. 15 (1978) 559–562, https://doi.org/10.1116/1.569472.
[10] D. Castner, B. Sexton, G. Somorjai, Leed and thermal desorption studies of small molecules (h2, o2, co, co2, no, c2h4, c2h2 and c) chemisorbed on the rhodium (111) and (100) surfaces, Surf. Sci. 71 (1978) 519–540, https://doi.org/10.1016/0039-6028(78)90444-2.
[11] A. Tontegode, Carbon on transition metal surfaces, Prog. Surf. Sci. 38 (1991) 201–429, https://doi.org/10.1016/0079-6816(91)90002-L.
[12] I. Pletikosić, M. Kralj, P. Pervan, R. Brako, J. Coraux, A.T. N'Diaye, C. Busse, T. Michely, Dirac cones and minigaps for graphene on ir(111), Phys. Rev. Lett. 102 (2009), 056808, https://doi.org/10.1103/PhysRevLett.102.056808.
[13] M. M. Otrokov, I. I. Klimovskikh, F. Calleja, A. M. Shikin, O. Vilkov, A. G. Rybkin, D. Estyunin, S. Muff, J. H. Dil, A. L. Vázquez de Parga, R. Miranda, H. Ochoa, F. Guinea, J. I. Cerda, E. V. Chulkov, A. Arnau, Evidence of large spin-orbit coupling effects in quasi-free-standing graphene on Pb/Ir(111), 2D Mater.. 5. doi:10.1088/2053-1583/aac596.
[14] F. Himpsel, K. Christmann, P. Heimann, D. Eastman, P.J. Feibelman, Adsorbate band dispersions for c on ru(0001), Surf. Sci. Lett. 115 (1982) L159–L164, https://doi.org/10.1016/0167-2584(82)90679-X.
[15] J. Hrbek, Carbonaceous overlayers on ru(001), J. Vac. Sci. Technol., A 4 (1986) 86–89, https://doi.org/10.1116/1.573460.
[16] J. Vaari, J. Lahtinen, P. Hautojarvi, The adsorption and decompositon of acetylene on clean and k-covered co(0001), Catal. Lett. 44 (1997) 43.
[17] N. Kholin, E. Rut'kov, A. Tontegode, The nature of the adsorption bond between graphite islands and iridium surface, Surf. Sci. 139 (1984) 155–172, https://doi.org/10.1016/0039-6028(84)90014-1.
[18] R. Rosei, S. Modesti, F. Sette, C. Quaresima, A. Savoia, P. Perfetti, Electronic structure of carbidic and graphitic carbon on ni(111), Phys. Rev. B 29 (1984) 3416–3422, https://doi.org/10.1103/PhysRevB.29.3416.
[19] D. Goodman, J. Yates, Co isotopic mixing measurements on nickel: evidence for irreversibility of co dissociation, J. Catal. 82 (1983) 255–260.
[20] T.A. Land, T. Michely, R.J. Behm, J.C. Hemminger, G. Comsa, Direct observation of surface reactions by scanning tunneling microscopy: ethylene ethylidyne carbon particles graphite on pt(111), J. Chem. Phys. 97 (1992) 6774–6783, https://doi.org/10.1063/1.463655.
[21] T. Land, T. Michely, R. Behm, J. Hemminger, G. Comsa, Stm investigation of single layer graphite structures produced on pt(111) by hydrocarbon decomposition, Surf. Sci. 264 (1992) 261–270, https://doi.org/10.1016/0039-6028(92)90183-7.
[22] C. Klink, I. Stensgaard, F. Besenbacher, E. Laegsgaard, An stm study of carbon-induced structure on ni(111): evidence for a carbidic-phase clock reconstruction, Surf. Sci. 342 (1995) 250.
[23] Y. Souzu, M. Tsukada, Electronic states and scanning tunneling spectroscopy image of monolayer graphite on a nickel (111) surface by the dv-x method, Surf. Sci. 326 (1995) 42–52, https://doi.org/10.1016/0039-6028(94)00558-3.
[24] M. Wu, Q. Xu, D. Goodman, Investigations of graphitic overlayers formed from methane decomposition on ru(0001) and ru(11.hivin.20) catalysts with scanning tunneling microscopy and high-resolution electron energy loss spectroscopy, J. Phys. Chem. 98 (19) (1994) 5104, https://doi.org/10.1021/j100070a027.
[25] J. Hamilton, J. Blakely, Carbon segregation to single crystal surfaces of pt, pd and co, Surf. Sci. 91 (1) (1980) 199–217, https://doi.org/10.1016/0039-6028(80)90080-1.
[26] P.J. Feibelman, Structure of carbidic and graphitic phases on ru(0001), Surf. Sci. 103 (1981) L149, https://doi.org/10.1016/0039-6028(81)90262-4. –L154.
[27] H. Zi-Pu, D. Ogletree, M.V. Hove, G. Somorjai, Leed theory for incommensurate overlayers: application to graphite on pt(111), Surf. Sci. 180 (1987) 433–459, https://doi.org/10.1016/0039-6028(87)90219-6.
[28] R. Rosei, M. De Crescenzi, R. Sette, C. Quaresima, A. Savoia, P. Perfetti, Structure of graphitic carbon on ni(111): a surface extended-energy-loss fine-structure study, Phys. Rev. B 28 (1983) 1161.
[29] L. Papagno, L.S. Caputi, Determination of graphitic carbon structure adsorbed on ni(110) by surface extended energy-loss fine-structure analysis, Phys. Rev. B 29 (1984) 1483–1486, https://doi.org/10.1103/PhysRevB.29.1483.
[30] C. McConville, D. Woodruff, S. Kevan, The electronic structure of graphitic overlayers on ni100, Surf. Sci. 171 (1986) L447–L453, https://doi.org/10.1016/0039-6028(86)91072-1.
[31] Y. Gamo, A. Nagashima, M. Wakabayashi, M. Terai, C. Oshima, Atomic structure of monolayer graphite formed on ni(111), Surf. Sci. 374 (1997) 61–64, https://doi.org/10.1016/S0039-6028(96)00785-6.
[32] H. Kawanowa, H. Ozawa, T. Yazaki, Y. Gotoh, R. Souda, Structure analysis of monolayer graphite on ni(111) surface by li^{+}-impact collision ion scattering spectroscopy, Jpn. J. Appl. Phys. 41 (2002) 6149–6152, https://doi.org/10.1143/jjap.41.6149.
[33] H. Itoh, T. Ichinose, C. Oshima, T. Ichinokawa, T. Aizawa, Scanning tunneling microscopy of monolayer graphite epitaxially grown on a tic(111) surface, Surf. Sci. 254 (1991) L437–L442, https://doi.org/10.1016/0039-6028(91)90620-8.
[34] M. Enachescu, D. Schleef, D.F. Ogletree, M. Salmeron, Integration of point-contact microscopy and atomic-force microscopy: application to characterization of graphite/pt(111), Phys. Rev. B 60 (1999) 16913–16919, https://doi.org/10.1103/PhysRevB.60.16913.
[35] M. Sasaki, Y. Yamada, Y. Ogiwara, S. Yagyu, S. Yamamoto, Moire contrast in the local tunneling barrier height images of monolayer graphite on pt(111), Phys. Rev. B 61 (2000) 15653–15656, https://doi.org/10.1103/PhysRevB.61.15653.
[36] T. Aizawa, R. Souda, S. Otani, Y. Ishizawa, Anomalous bond of monolayer graphite on transition-metal carbide surface, Phys. Rev. Lett. 64 (7) (1990) 678.
[37] T. Aizawa, Y. Hwang, W. Hayami, R. Souda, S. Otani, Y. Ishizawa, Phonon dispersion of monolayer graphite on pt(111) and nbc surfaces: bond softening and interface structures, Surf. Sci. 260 (1992) 311–318, https://doi.org/10.1016/0039-6028(92)90046-9.
[38] Y. Hwang, T. Aizawa, W. Hayami, S. Otani, Y. Ishizawa, S.-J. Park, Surface phonon and electronic structure of a graphite monolayer formed on zrc(111) and (001) surfaces, Surf. Sci. 271 (1992) 299–307, https://doi.org/10.1016/0039-6028(92)90886-B.
[39] A. Nagashima, N. Tejima, C. Oshima, Electronic states of the pristine and alkali-metal-intercalated monolayer graphite/ni(111) systems, Phys. Rev. B 50 (23) (1994) 487.
[40] A.M. Shikin, D. Farías, K.H. Rieder, Phonon stiffening induced by copper intercalation in monolayer graphite on ni(111), Europhys. Lett. 44 (1998) 44–49, https://doi.org/10.1209/epl/i1998-00432-x.
[41] A. Shikin, D. Farías, V. Adamchuk, K.-H. Rieder, Surface phonon dispersion of a graphite monolayer adsorbed on ni(111) and its modification caused by intercalation of yb, la and cu layers, Surf. Sci. 424 (1999) 155–167, https://doi.org/10.1016/S0039-6028(99)00099-0.
[42] D. Farías, A.M. Shikin, K.-H. Rieder, Y.S. Dedkov, Synthesis of a weakly bonded graphite monolayer on ni(111) by intercalation of silver, J. Phys. Condens. Matter 11 (1999) 8453–8458, https://doi.org/10.1088/0953-8984/11/43/308.
[43] N.R. Gall', E. Rut'kov, A. Tontegode, Y.N. Tsarev, Simultaneous intercalation of cesium and potassium atoms into a two-dimensional graphite film on ir(111, JETP Lett. 71 (2000) 457–459, https://doi.org/10.1134/1.1307992.
[44] E.V. Rut'kov, A.Y. Tontegode, M.M. Usufov, Evidence for a c_{60} monolayer intercalated between a graphite monolayer and iridium, Phys. Rev. Lett. 74 (1995) 758–760, https://doi.org/10.1103/PhysRevLett.74.758.
[45] A. Shikin, Y. Dedkov, V. Adamchuk, D. Farías, K. Rieder, Formation of an intercalation-like system by intercalation of c60 molecules underneath a graphite monolayer on ni(111), Surf. Sci. 452 (1) (2000) 1–8, https://doi.org/10.1016/S0039-6028(00)00291-0.
[46] G. Hong, Q.-H. Wu, J. Ren, C. Wang, W. Zhang, S.-T. Lee, Recent progress in organic molecule/graphene interfaces, Nano Today 8 (2013) 388–402, https://doi.org/10.1016/j.nantod.2013.07.003.
[47] L. Kong, A. Enders, T.S. Rahman, P.A. Dowben, Molecular adsorption on graphene, J. Phys. Condens. Matter 26 (2014), 443001, https://doi.org/10.1088/0953-8984/26/44/443001.
[48] J.M. MacLeod, F. Rosei, Molecular self-assembly on graphene, Small 10 (2014) 1038–1049, https://doi.org/10.1002/smll.201301982.
[49] A. Kumar, K. Banerjee, P. Liljeroth, Molecular assembly on two-dimensional materials, Nanotechnology 28 (2017), 082001, https://doi.org/10.1088/1361-6528/aa564f.
[50] S. Feng, N. Luo, A. Tang, W. Chen, Y. Zhang, S. Huang, W. Dou, Phthalocyanine and metal phthalocyanines adsorbed on graphene: a density functional study, J. Phys. Chem. C 123 (2019) 16614–16620, https://doi.org/10.1021/acs.jpcc.8b11757.
[51] J. Cho, J. Smerdon, L. Gao, O. Suzer, J.R. Guest, N.P. Guisinger, Structural and electronic decoupling of c60 from epitaxial graphene on sic, Nano Lett. 12 (2012) 3018–3024, https://doi.org/10.1021/nl3008049.
[52] P. Jrvinen, S.K. Hmlinen, K. Banerjee, P. Hkkinen, M. Ijs, A. Harju, P. Liljeroth, Molecular self-assembly on graphene on sio2 and h-bn substrates, Nano Lett. 13 (2013) 3199–3204, https://doi.org/10.1021/nl401265f.
[53] H. Huang, S. Chen, X. Gao, W. Chen, A.T.S. Wee, Structural and electronic properties of ptcda thin films on epitaxial graphene, ACS Nano 3 (2009) 3431–3436, https://doi.org/10.1021/nn9008615.
[54] M. Švec, P. Merino, Y.J. Dappe, C. González, E. Abad, P. Jelínek, J.A. Martín-Gago, Van der waals interactions mediating the cohesion of fullerenes on graphene, Phys. Rev. B 86 (2012), 121407, https://doi.org/10.1103/PhysRevB.86.121407.
[55] G. Hlawacek, F.S. Khokhar, R. van Gastel, B. Poelsema, C. Teichert, Smooth growth of organic semiconductor films on graphene for high-efficiency electronics, Nano Lett. 11 (2011) 333–337, https://doi.org/10.1021/nl103739n.
[56] A. Rochefort, J.D. Wuest, Interaction of substituted aromatic compounds with graphene, Langmuir 25 (2009) 210–215, https://doi.org/10.1021/la802284j.
[57] Y.-L. Wang, J. Ren, C.-L. Song, Y.-P. Jiang, L.-L. Wang, K. He, X. Chen, J.-F. Jia, S. Meng, E. Kaxiras, Q.-K. Xue, X.-C. Ma, Selective adsorption and electronic

interaction of $f_{16}cupc$ on epitaxial graphene, Phys. Rev. B 82 (2010), 245420, https://doi.org/10.1103/PhysRevB.82.245420.
[58] Q.H. Wang, M.C. Hersam, Room-temperature molecular-resolution characterization of self-assembled organic monolayers on epitaxial graphene, Nat. Chem. 1 (2009) 206–211, https://doi.org/10.1038/NCHEM.212.
[59] Y.H. Lu, W. Chen, Y.P. Feng, P.M. He, Tuning the electronic structure of graphene by an organic molecule, J. Phys. Chem. B 113 (2009) 2–5, https://doi.org/10.1021/jp806905e.
[60] H. Pinto, R. Jones, J.P. Goss, P.R. Briddon, p-type doping of graphene with f4-TCNQ, J. Phys. Condens. Matter 21 (2009), 402001.
[61] W. Chen, S. Chen, D.C. Qi, X.Y. Gao, A.T.S. Wee, Surface transfer p-type doping of epitaxial graphene, J. Am. Chem. Soc. 129 (2007) 10418–10422, https://doi.org/10.1021/ja071658g.
[62] C. Coletti, C. Riedl, D.S. Lee, B. Krauss, L. Patthey, K. von Klitzing, J.H. Smet, U. Starke, Charge neutrality and band-gap tuning of epitaxial graphene on sic by molecular doping, Phys. Rev. B 81 (2010), 235401, https://doi.org/10.1103/PhysRevB.81.235401.
[63] J.T. Sun, Y.H. Lu, W. Chen, Y.P. Feng, A.T.S. Wee, Linear tuning of charge carriers in graphene by organic molecules and charge-transfer complexes, Phys. Rev. B 81 (2010), 155403, https://doi.org/10.1103/PhysRevB.81.155403.
[64] Y.-H. Zhang, K.-G. Zhou, K.-F. Xie, J. Zeng, H.-L. Zhang, Y. Peng, Tuning the electronic structure and transport properties of graphene by noncovalent functionalization: effects of organic donor, acceptor and metal atoms, Nanotechnology 21 (2010), 065201.
[65] X.Q. Tian, J.B. Xu, X.M. Wang, Self-assembly of ptcda ultrathin films on graphene: structural phase transition and charge transfer saturation, J. Phys. Chem. C 114 (2010) 20917–20924, https://doi.org/10.1021/jp1031674.
[66] D. Choudhury, B. Das, D. Sarma, C. Rao, Xps evidence for molecular charge-transfer doping of graphene, Chem. Phys. Lett. 497 (2010) 66–69, https://doi.org/10.1016/j.cplett.2010.07.089.
[67] Z. Zhang, H. Huang, X. Yang, L. Zang, Tailoring electronic properties of graphene by stacking with aromatic molecules, J. Phys. Chem. Lett. 2 (2011) 2897–2905, https://doi.org/10.1021/jz201273r.
[68] H.J. Karmel, J.J. Garramone, J.D. Emery, S. Kewalramani, M.J. Bedzyk, M. C. Hersam, Self-assembled organic monolayers on epitaxial graphene with enhanced structural and thermal stability, Chem. Commun. 50 (2014) 8852–8855, https://doi.org/10.1039/C4CC02761B.
[69] Q. Su, S. Pang, V. Alijani, C. Li, X. Feng, K. Mllen, Composites of graphene with large aromatic molecules, Adv. Mater. 21 (2009) 3191–3195, https://doi.org/10.1002/adma.200803808.
[70] X. Dong, D. Fu, W. Fang, Y. Shi, P. Chen, L.-J. Li, Doping single-layer graphene with aromatic molecules, Small 5 (2009) 1422–1426, https://doi.org/10.1002/smll.200801711.
[71] J. Hong, E. Bekyarova, W.A. de Heer, R.C. Haddon, S. Khizroev, Chemically engineered graphene-based 2d organic molecular magnet, ACS Nano 7 (2013) 10011–10022, https://doi.org/10.1021/nn403939r.
[72] Q.H. Wang, M.C. Hersam, Nanofabrication of heteromolecular organic nanostructures on epitaxial graphene via room temperature feedback-controlled lithography, Nano Lett. 11 (2011) 589–593, https://doi.org/10.1021/nl103590j.
[73] J. Wintterlin, M.-L. Bocquet, Graphene on metal surfaces, Surf. Sci. 603 (2009) 1841–1852, https://doi.org/10.1016/j.susc.2008.08.037.
[74] A.B. Preobrajenski, M.L. Ng, A.S. Vinogradov, N. Mårtensson, Controlling graphene corrugation on lattice-mismatched substrates, Phys. Rev. B 78 (2008), 073401, https://doi.org/10.1103/PhysRevB.78.073401.
[75] M. Batzill, The surface science of graphene: metal interfaces, CVD synthesis, nanoribbons, chemical modifications, and defects, Surf. Sci. Rep. 67 (2012) 83–115, https://doi.org/10.1016/j.surfrep.2011.12.001.
[76] G.A. Somorjai, Modern surface science and surface technologies: an introduction, Chem. Rev. 96 (1996) 1223–1236, https://doi.org/10.1021/cr950234e.
[77] K. Lasek, J. Li, S. Kolekar, P.M. Coelho, L. Guo, M. Zhang, Z. Wang, M. Batzill, Synthesis and characterization of 2D transition metal dichalcogenides: recent progress from a vacuum surface science perspective, Surf. Sci. Rep. 76 (2021), 100523, https://doi.org/10.1016/j.surfrep.2021.100523.
[78] J.J. Navarro, S. Leret, F. Calleja, D. Stradi, A. Black, R. Bernardo-Gavito, M. Garnica, D. Granados, A.L. Vázquez de Parga, E.M. Pérez, R. Miranda, Organic covalent patterning of nanostructured graphene with selectivity at the atomic level, Nano Lett. 16 (2016) 355–361, https://doi.org/10.1021/acs.nanolett.5b03928.
[79] F. Jona, J.A. Strozier, W.S. Yang, Low-energy electron diffraction for surface structure analysis, Rep. Prog. Phys. 45 (1982) 527–585, https://doi.org/10.1088/0034-4885/45/5/002.
[80] I. Tilinin, Quantitative surface analysis by Auger and x-ray photoelectron spectroscopy, Prog. Surf. Sci. 52 (1996) 193–335, https://doi.org/10.1016/0079-6816(96)00008-1.
[81] G. Greczynski, L. Hultman, X-ray photoelectron spectroscopy: towards reliable binding energy referencing, Prog. Mater. Sci. 107 (2020), 100591, https://doi.org/10.1016/j.pmatsci.2019.100591.
[82] A. Damascelli, Probing the electronic structure of complex systems by ARPES, Phys. Scripta T109 (2004) 61, https://doi.org/10.1238/Physica.Topical.109a00061.
[83] F. Reinert, S. Hüfner, Photoemission spectroscopy—from early days to recent applications, New J. Phys. 7 (2005), https://doi.org/10.1088/1367-2630/7/1/097, 97–97.
[84] G. Binnig, H. Rohrer, C. Gerber, E. Weibel, Surface studies by scanning tunneling microscopy, Phys. Rev. Lett. 49 (1982) 57–61, https://doi.org/10.1103/PhysRevLett.49.57.
[85] J. Tersoff, D.R. Hamann, Theory and application for the scanning tunneling microscope, Phys. Rev. Lett. 50 (1983) 1998–2001, https://doi.org/10.1103/PhysRevLett.50.1998.
[86] J. Tersoff, D.R. Hamann, Theory of the scanning tunneling microscope, Phys. Rev. B 31 (1985) 805–813, https://doi.org/10.1103/PhysRevB.31.805.
[87] N.D. Lang, Spectroscopy of single atoms in the scanning tunneling microscope, Phys. Rev. B 34 (1986) 5947–5950, https://doi.org/10.1103/PhysRevB.34.5947.
[88] F. Calleja, A. Arnau, J.J. Hinarejos, A.L. Vázquez de Parga, W.A. Hofer, P. M. Echenique, R. Miranda, Contrast reversal and shape changes of atomic adsorbates measured with scanning tunneling microscopy, Phys. Rev. Lett. 92 (2004), 206101, https://doi.org/10.1103/PhysRevLett.92.206101.
[89] M. Bode, Spin-polarized scanning tunnelling microscopy, Rep. Prog. Phys. 66 (2003) 523–582, https://doi.org/10.1088/0034-4885/66/4/203.
[90] P.K. Hansma, J. Tersoff, Scanning tunneling microscopy, J. Appl. Phys. 61 (1987) 24.
[91] J.E. Griffith, G.P. Kochanski, Scanning tunneling microscopy, Annu. Rev. Mater. Sci. 20 (1990) 27.
[92] L.E.C. van de Leemput, H. van Kempen, Scanning tunnelling microscopy, Rep. Prog. Phys. 55 (1992) 1165–1240, https://doi.org/10.1088/0034-4885/55/8/002.
[93] F. Besenbacher, J. Lauritsen, T. Linderoth, E. Lægsgaard, R. Vang, S. Wendt, Atomic-scale surface science phenomena studied by scanning tunneling microscopy, Surf. Sci. 603 (2009) 1315–1327, https://doi.org/10.1016/j.susc.2008.08.038.
[94] E.Y. Andrei, G. Li, X. Du, Electronic properties of graphene: a perspective from scanning tunneling microscopy and magnetotransport, Rep. Prog. Phys. 75 (2012), 056501, https://doi.org/10.1088/0034-4885/75/5/056501.
[95] J. Schwenk, S. Kim, J. Berwanger, F. Ghahari, D. Walkup, M.R. Slot, S.T. Le, W. G. Cullen, S.R. Blankenship, S. Vranjkovic, H.J. Hug, Y. Kuk, F.J. Giessibl, J. A. Stroscio, Achieving μ eV tunneling resolution in an *in-operando* scanning tunneling microscopy, atomic force microscopy, and magnetotransport system for quantum materials research, Rev. Sci. Instrum. 91 (2020), 071101, https://doi.org/10.1063/5.0005320.
[96] B. Borca, S. Barja, M. Garnica, M. Minniti, A. Politano, J.M. Rodríguez-García, J. J. Hinarejos, D. Farías, A.L.V. de Parga, R. Miranda, Electronic and geometric corrugation of periodically rippled, self-nanostructured graphene epitaxially grown on ru(0001), New J. Phys. 12 (2010), 093018, https://doi.org/10.1088/1367-2630/12/9/093018.
[97] Q. Dubout, F. Calleja, G. Sclauzero, M. Etzkorn, A. Lehnert, L. Claude, M. Papagno, F.D. Natterer, F. Patthey, S. Rusponi, A. Pasquarello, H. Brune, Giant apparent lattice distortions in STM images of corrugated sp ^{2} -hybridised monolayers, New J. Phys. 18 (10) (2016), 103027, https://doi.org/10.1088/1367-2630/18/10/103027.
[98] D. Martoccia, P.R. Willmott, T. Brugger, M. Björck, S. Günther, C.M. Schlepütz, A. Cervellino, S.A. Pauli, B.D. Patterson, S. Marchini, J. Wintterlin, W. Moritz, T. Greber, Graphene on ru(0001): a 25 × 25 supercell, Phys. Rev. Lett. 101 (2008), 126102, https://doi.org/10.1103/PhysRevLett.101.126102.
[99] W. Moritz, B. Wang, M.-L. Bocquet, T. Brugger, T. Greber, J. Wintterlin, S. Günther, Structure determination of the coincidence phase of graphene on ru (0001), Phys. Rev. Lett. 104 (2010), 136102, https://doi.org/10.1103/PhysRevLett.104.136102.
[100] M. Iannuzzi, I. Kalichava, H. Ma, S.J. Leake, H. Zhou, G. Li, Y. Zhang, O. Bunk, H. Gao, J. Hutter, P.R. Willmott, T. Greber, Moiré beatings in graphene on Ru (0001), Phys. Rev. B 88 (12) (2013), 125433, https://doi.org/10.1103/PhysRevB.88.125433.
[101] A.T. N'Diaye, S. Bleikamp, P.J. Feibelman, T. Michely, Two-dimensional ir cluster lattice on a graphene moire on ir(111), Phys. Rev. Lett. 97 (2006), 215501, https://doi.org/10.1103/PhysRevLett.97.215501.
[102] A.T. N'Diaye, J. Coraux, T.N. Plasa, C. Busse, T. Michely, Structure of epitaxial graphene on ir(111), New J. Phys. 10 (2008), 043033, https://doi.org/10.1088/1367-2630/10/4/043033.
[103] C. Romero-Muñiz, A. Martín-Recio, P. Pou, J.M. Gómez-Rodrí-guez, R. Pérez, Substrate-induced enhancement of the chemical reactivity in metal-supported graphene, Phys. Chem. Chem. Phys. 20 (2018) 19492–19499, https://doi.org/10.1039/C8CP02827C.
[104] H.J. Monkhorst, J.D. Pack, Special points for brillouin-zone integrations, Phys. Rev. B 13 (1976) 5188–5192, https://doi.org/10.1103/PhysRevB.13.5188.
[105] D.J. Chadi, M.L. Cohen, Special points in the brillouin zone, Phys. Rev. B 8 (1973) 5747–5753, https://doi.org/10.1103/PhysRevB.8.5747.
[106] D.R. Hamann, M. Schlüter, C. Chiang, Norm-conserving pseudopotentials, Phys. Rev. Lett. 43 (1979) 1494–1497, https://doi.org/10.1103/PhysRevLett.43.1494.
[107] D. Vanderbilt, Soft self-consistent pseudopotentials in a generalized eigenvalue formalism, Phys. Rev. B 41 (1990) 7892–7895, https://doi.org/10.1103/PhysRevB.41.7892.
[108] P.E. Blöchl, Projector augmented-wave method, Phys. Rev. B 50 (1994) 17953–17979, https://doi.org/10.1103/PhysRevB.50.17953.
[109] https://www.quantum-espresso.org/.
[110] https://diamond.kist.re.kr/CSC/code/dacapo.
[111] https://www.vasp.at/.
[112] https://www.scm.com/product/adf/.
[113] https://www.crystal.unito.it/index.php.
[114] https://departments.icmab.es/leem/siesta/.
[115] P. Sony, P. Puschnig, D. Nabok, C. Ambrosch-Draxl, Importance of van der waals interaction for organic molecule-metal junctions: adsorption of thiophene on cu (110) as a prototype, Phys. Rev. Lett. 99 (2007), 176401, https://doi.org/10.1103/PhysRevLett.99.176401.

[116] N. Atodiresei, V. Caciuc, P. Lazić, S. Blügel, Chemical versus van der waals interaction: the role of the heteroatom in the flat absorption of aromatic molecules c_6h_6, c_5nh_5, and $c_4n_2h_4$ on the cu(110) surface, Phys. Rev. Lett. 102 (2009), 136809, https://doi.org/10.1103/PhysRevLett.102.136809.
[117] J. Brede, N. Atodiresei, S. Kuck, P. Lazić, V. Caciuc, Y. Morikawa, G. Hoffmann, S. Blügel, R. Wiesendanger, Spin- and energy-dependent tunneling through a single molecule with intramolecular spatial resolution, Phys. Rev. Lett. 105 (2010), 047204, https://doi.org/10.1103/PhysRevLett.105.047204.
[118] G. Mercurio, E.R. McNellis, I. Martin, S. Hagen, F. Leyssner, S. Soubatch, J. Meyer, M. Wolf, P. Tegeder, F.S. Tautz, K. Reuter, Structure and energetics of azobenzene on ag(111): benchmarking semiempirical dispersion correction approaches, Phys. Rev. Lett. 104 (2010), 036102, https://doi.org/10.1103/PhysRevLett.104.036102.
[119] M. Mura, A. Gulans, T. Thonhauser, L. Kantorovich, Role of van der waals interaction in forming molecule-metal junctions: flat organic molecules on the au (111) surface, Phys. Chem. Chem. Phys. 12 (2010) 4759–4767, https://doi.org/10.1039/B920121A.
[120] E.R. McNellis, C. Bronner, J. Meyer, M. Weinelt, P. Tegeder, K. Reuter, Azobenzene versus 3,3,5,5-tetra-tert-butyl-azobenzene (tba) at au(111): characterizing the role of spacer groups, Phys. Chem. Chem. Phys. 12 (2010) 6404–6412, https://doi.org/10.1039/C001978J.
[121] F. Libisch, C. Huang, P. Liao, M. Pavone, E.A. Carter, Origin of the energy barrier to chemical reactions of o_2 on al(111): evidence for charge transfer, not spin selection, Phys. Rev. Lett. 109 (2012), 198303, https://doi.org/10.1103/PhysRevLett.109.198303.
[122] J. Cheng, F. Libisch, E.A. Carter, Dissociative adsorption of o2 on al(111): the role of orientational degrees of freedom, J. Phys. Chem. Lett. 6 (2015) 1661–1665, https://doi.org/10.1021/acs.jpclett.5b00597.
[123] B. Wang, M.-L. Bocquet, S. Marchini, S. Gunther, J. Wintterlin, Chemical origin of a graphene moire overlayer on ru(0001), Phys. Chem. Chem. Phys. 10 (2008) 3530–3534, https://doi.org/10.1039/B801785A.
[124] B. Wang, M.-L. Bocquet, S. Günther, J. Wintterlin, Comment on "periodically rippled graphene: growth and spatially resolved electronic structure", Phys. Rev. Lett. 101 (2008), 099703 https://doi.org/10.1103/PhysRevLett.101.099703.
[125] D.-E. Jiang, M.-H. Du, S. Dai, First principles study of the graphene/ru(0001) interface, J. Chem. Phys. 130 (2009), 074705, https://doi.org/10.1063/1.3077295.
[126] B. Wang, M. Caffio, C. Bromley, H. Fruchtl, R. Schaub, Coupling epitaxy, chemical bonding, and work function at the local scale in transition metal-supported graphene, ACS Nano 4 (2010) 5773–5782, https://doi.org/10.1021/nn101520k.
[127] D. Martoccia, M. Bjorck, C.M. Schlepuetz, T. Brugger, S.A. Pauli, B.D. Patterson, T. Greber, P.R. Willmott, Graphene on ru(0001): a corrugated and chiral structure, New J. Phys. 12 (2010), 043028, https://doi.org/10.1088/1367-2630/12/4/043028.
[128] A.L. Vázquez de Parga, F. Calleja, B. Borca, M.C.G. Passeggi, J.J. Hinarejos, F. Guinea, R. Miranda, Vázquez de parga et al. reply, Phys. Rev. Lett. 101 (2008), 099704, https://doi.org/10.1103/PhysRevLett.101.099704.
[129] D. Stradi, S. Barja, C. Díaz, M. Garnica, B. Borca, J.J. Hinarejos, D. Sánchez-Portal, M. Alcamí, A. Arnau, A.L. Vázquez de Parga, R. Miranda, F. Martín, Role of dispersion forces in the structure of graphene monolayers on ru surfaces, Phys. Rev. Lett. 106 (2011), 186102, https://doi.org/10.1103/PhysRevLett.106.186102.
[130] S. Grimme, Accurate description of van der waals complexes by density functional theory including empirical corrections, J. Comput. Chem. 25 (12) (2004) 1463–1473, https://doi.org/10.1002/jcc.20078.
[131] S. Grimme, Semiempirical gga-type density functional constructed with a long-range dispersion correction, J. Comput. Chem. 27 (15) (2006) 1787–1799, https://doi.org/10.1002/jcc.20495.
[132] M. D. Jímenez-Sánchez, N. Nicoara, J. M. Gómez-Rodríguez, Chemical identification with non-contact atomic force microscopy of xenon atoms adsorbed on graphene on Pt(111) surfaces, Appl. Surf. Sci. 542. doi:10.1016/j.apsusc.2020.148669.
[133] S. Grimme, J. Antony, S. Ehrlich, H. Krieg, A consistent and accurate ab initio parametrization of density functional dispersion correction (dft-d) for the 94 elements h-pu, J. Chem. Phys. 132 (2010), 154104, https://doi.org/10.1063/1.3382344.
[134] A. Tkatchenko, M. Scheffler, Accurate molecular van der waals interactions from ground-state electron density and free-atom reference data, Phys. Rev. Lett. 102 (2009), 073005, https://doi.org/10.1103/PhysRevLett.102.073005.
[135] V.G. Ruiz, W. Liu, E. Zojer, M. Scheffler, A. Tkatchenko, Density-functional theory with screened van der waals interactions for the modeling of hybrid inorganic-organic systems, Phys. Rev. Lett. 108 (2012), 146103, https://doi.org/10.1103/PhysRevLett.108.146103.
[136] A. Tkatchenko, R.A. DiStasio, R. Car, M. Scheffler, Accurate and efficient method for many-body van der waals interactions, Phys. Rev. Lett. 108 (2012), 236402, https://doi.org/10.1103/PhysRevLett.108.236402.
[137] J.J. Navarro, M. Pisarra, B. Nieto-Ortega, J. Villalva, C.G. Ayani, C. Díaz, F. Calleja, R. Miranda, F. Martín, E.M. Pérez, A.L.V. de Parga, Graphene catalyzes the reversible formation of a c–c bond between two molecules, Sci. Adv. 4 (2018), https://doi.org/10.1126/sciadv.aau9366 eaau9366.
[138] M. Dion, H. Rydberg, E. Schröder, D.C. Langreth, B.I. Lundqvist, Van der waals density functional for general geometries, Phys. Rev. Lett. 92 (2004), 246401, https://doi.org/10.1103/PhysRevLett.92.246401.
[139] J. Klimeš, D.R. Bowler, A. Michaelides, Chemical accuracy for the van der waals density functional, J. Phys.: cond. Matt. 22 (2009), 022201, https://doi.org/10.1088/0953-8984/22/2/022201.
[140] J.c. v. Klimeš, D.R. Bowler, A. Michaelides, Van der waals density functionals applied to solids, Phys. Rev. B 83 (2011), 195131, https://doi.org/10.1103/PhysRevB.83.195131.
[141] K. Lee, E.D. Murray, L. Kong, B.I. Lundqvist, D.C. Langreth, Higher-accuracy van der waals density functional, Phys. Rev. B 82 (2010), 081101, https://doi.org/10.1103/PhysRevB.82.081101.
[142] O.A. Vydrov, T. Van Voorhis, Nonlocal van der waals density functional made simple, Phys. Rev. Lett. 103 (2009), 063004, https://doi.org/10.1103/PhysRevLett.103.063004.
[143] D.C. Langreth, B.I. Lundqvist, Comment on "nonlocal van der waals density functional made simple", Phys. Rev. Lett. 104 (2010), 099303 https://doi.org/10.1103/PhysRevLett.104.099303.
[144] O.A. Vydrov, T. Van Voorhis, Vydrov and van voorhis reply, Phys. Rev. Lett. 104 (2010), 099304, https://doi.org/10.1103/PhysRevLett.104.099304.
[145] G. Román-Pérez, J.M. Soler, Efficient implementation of a van der waals density functional: application to double-wall carbon nanotubes, Phys. Rev. Lett. 103 (2009), 096102, https://doi.org/10.1103/PhysRevLett.103.096102.
[146] W. Tang, E. Sanville, G. Henkelman, A grid-based bader analysis algorithm without lattice bias, J. Phys. Condens. Matter 21 (2009), 084204, https://doi.org/10.1088/0953-8984/21/8/084204.
[147] R.F.W. Bader, A quantum theory of molecular structure and its applications, Chem. Rev. 91 (1991) 893–928, https://doi.org/10.1021/cr00005a013.
[148] D. Stradi, M. Garnica, C. Díaz, F. Calleja, S. Barja, N. Martín, M. Alcamí, A. L. Vázquez de Parga, R. Miranda, F. Martín, Controlling the spatial arrangement of organic magnetic anions adsorbed on epitaxial graphene on ru(0001), Nanoscale 6 (2014) 15271–15279, https://doi.org/10.1039/C4NR02917H.
[149] J. Bardeen, Tunneling from a many-particle points of view, Phys. Rev. Lett. 6 (1961) 57, https://doi.org/10.1016/0039-6028(69)90227-1.
[150] C.J. Chen, Origin of atomic resolution on metal surfaces in scanning tunneling microscopy, Phys. Rev. Lett. 65 (1990) 448–451, https://doi.org/10.1103/PhysRevLett.65.448.
[151] W.A. Hofer, A.S. Foster, A.L. Shluger, Theories of scanning probe microscopes at the atomic scale, Rev. Mod. Phys. 75 (2003) 1287–1331, https://doi.org/10.1103/RevModPhys.75.1287.
[152] J.M. Blanco, F. Flores, R. Pérez, Stm-theory: image potential, chemistry and surface relaxation, Prog. Surf. Sci. 81 (2006) 403–443, https://doi.org/10.1016/j.progsurf.2006.07.004.
[153] J. Coraux, A.T. N'Diaye, C. Busse, T. Michely, Structural coherency of graphene on ir(111), Nano Lett. 8 (2008) 565–570, https://doi.org/10.1021/nl0728874.
[154] E. Loginova, N.C. Bartelt, P.J. Feibelman, K.F. McCarty, Factors influencing graphene growth on metal surfaces, New J. Phys. 11 (2009), 063046, https://doi.org/10.1088/1367-2630/11/6/063046.
[155] S. Marchini, S. Günther, J. Wintterlin, Scanning tunneling microscopy of graphene on ru(0001), Phys. Rev. B 76 (2007), 075429, https://doi.org/10.1103/PhysRevB.76.075429.
[156] A.L. Vázquez de Parga, F. Calleja, B. Borca, M.C.G. Passeggi, J.J. Hinarejos, F. Guinea, R. Miranda, Periodically rippled graphene: growth and spatially resolved electronic structure, Phys. Rev. Lett. 100 (2008), 056807, https://doi.org/10.1103/PhysRevLett.100.056807.
[157] A.L. Vázquez de Parga, F. Calleja, B. Borca, M.C.G. Passeggi, J.J. Hinarejos, F. Guinea, R. Miranda, Vázquez de parga et al. reply, Phys. Rev. Lett. 101 (2008), 099704, https://doi.org/10.1103/PhysRevLett.101.099704.
[158] Y. Pan, H. Zhang, D. Shi, J. Sun, S. Du, F. Liu, H. jun Gao, Highly ordered, millimeter-scale, continuous, single-crystalline graphene monolayer formed on ru (0001), Adv. Mater. 21 (2008) 2777–2780, https://doi.org/10.1002/adma.200800761.
[159] P.W. Sutter, J.-I. Flege, E.A. Sutter, Epitaxial graphene on ruthenium, Nat. Mater. 7 (2008) 406–411, https://doi.org/10.1038/nmat2166.
[160] H. Zhang, Q. Fu, Y. Cui, D. Tan, X. Bao, Growth mechanism of graphene on ru (0001) and o2 adsorption on the graphene/ru(0001) surface, J. Phys. Chemistry C 113 (2009) 8296–8301, https://doi.org/10.1021/jp810514u.
[161] T. Brugger, S. Günther, B. Wang, J.H. Dil, M.-L. Bocquet, J. Osterwalder, J. Wintterlin, T. Greber, Comparison of electronic structure and template function of single-layer graphene and a hexagonal boron nitride nanomesh on ru(0001), Phys. Rev. B 79 (2009), 045407, https://doi.org/10.1103/PhysRevB.79.045407.
[162] P. Sutter, J.T. Sadowski, E. Sutter, Graphene on pt(111): growth and substrate interaction, Phys. Rev. B 80 (2009), 245411, https://doi.org/10.1103/PhysRevB.80.245411.
[163] G. Otero, C. González, A.L. Pinardi, P. Merino, S. Gardonio, S. Lizzit, M. Blanco-Rey, K. Van de Ruit, C.F.J. Flipse, J. Méndez, P.L. de Andrés, J.A. Martín-Gago, Ordered vacancy network induced by the growth of epitaxial graphene on pt (111), Phys. Rev. Lett. 105 (2010), 216102, https://doi.org/10.1103/PhysRevLett.105.216102.
[164] M. Gao, Y. Pan, L. Huang, H. Hu, L.Z. Zhang, H.M. Guo, S.X. Du, H.-J. Gao, Epitaxial growth and structural property of graphene on pt(111), Appl. Phys. Lett. 98 (2011), 033101, https://doi.org/10.1063/1.3543624.
[165] A. Varykhalov, J. Sánchez-Barriga, A.M. Shikin, C. Biswas, E. Vescovo, A. Rybkin, D. Marchenko, O. Rader, Electronic and magnetic properties of quasifreestanding graphene on ni, Phys. Rev. Lett. 101 (2008), 157601, https://doi.org/10.1103/PhysRevLett.101.157601.
[166] L. Gao, J.R. Guest, N.P. Guisinger, Epitaxial graphene on cu(111), Nano Lett. 10 (2010) 3512–3516, https://doi.org/10.1021/nl1016706.
[167] E. Miniussi, M. Pozzo, A. Baraldi, E. Vesselli, R.R. Zhan, G. Comelli, T.O. Menteş, M.A. Niño, A. Locatelli, S. Lizzit, D. Alfè, Thermal stability of corrugated epitaxial graphene grown on re(0001), Phys. Rev. Lett. 106 (2011), 216101, https://doi.org/10.1103/PhysRevLett.106.216101.

[168] D. Eom, D. Prezzi, K.T. Rim, H. Zhou, M. Lefenfeld, S. Xiao, C. Nuckolls, M. S. Hybertsen, T.F. Heinz, G.W. Flynn, Structure and electronic properties of graphene nanoislands on co(0001), Nano Lett. 9 (2009) 2844–2848, https://doi.org/10.1021/nl900927f.
[169] A. Varykhalov, O. Rader, Graphene grown on co(0001) films and islands: electronic structure and its precise magnetization dependence, Phys. Rev. B 80 (2009), 035437, https://doi.org/10.1103/PhysRevB.80.035437.
[170] P. Merino, M. Svec, A.L. Pinardi, G. Otero, J.A. Martín-Gago, Strain-driven moire superstructures of epitaxial graphene on transition metal surfaces, ACS Nano 5 (2011) 5627–5634, https://doi.org/10.1021/nn201200j.
[171] A.B. Preobrajenski, M.L. Ng, A.S. Vinogradov, N. Mårtensson, Controlling graphene corrugation on lattice-mismatched substrates, Phys. Rev. B 78 (2008), 073401, https://doi.org/10.1103/PhysRevB.78.073401.
[172] B. Borca, S. Barja, M. Garnica, J.J. Hinarejos, A.L. Vázquez de Parga, R. Miranda, F. Guinea, Periodically modulated geometric and electronic structure of graphene on ru(0 0 0 1), Semicond. Sci. Technol. 25 (2010), 034001, https://doi.org/10.1088/0268-1242/25/3/034001.
[173] D. Stradi, S. Barja, C. Díaz, M. Garnica, B. Borca, J.J. Hinarejos, D. Sánchez-Portal, M. Alcamí, A. Arnau, A.L. Vázquez de Parga, R. Miranda, F. Martín, Electron localization in epitaxial graphene on ru(0001) determined by moire corrugation, Phys. Rev. B 85 (2012), 121404, https://doi.org/10.1103/PhysRevB.85.121404.
[174] G. Binnig, K.H. Frank, H. Fuchs, N. Garcia, B. Reihl, H. Rohrer, F. Salvan, A. R. Williams, Tunneling spectroscopy and inverse photoemission: image and field states, Phys. Rev. Lett. 55 (1985) 991–994, https://doi.org/10.1103/PhysRevLett.55.991.
[175] B. Borca, S. Barja, M. Garnica, D. Sánchez-Portal, V.M. Silkin, E.V. Chulkov, C. F. Hermanns, J.J. Hinarejos, A.L.V. de Parga, A. Arnau, P.M. Echenique, R. Miranda, Potential energy landscape for hot electrons in periodically nanostructured graphene, Phys. Rev. Lett. 105 (2010), 036804, https://doi.org/10.1103/physrevlett.105.036804.
[176] Y.S. Dedkov, A.M. Shikin, V.K. Adamchuk, S.L. Molodtsov, C. Laubschat, A. Bauer, G. Kaindl, Intercalation of copper underneath a monolayer of graphite on ni(111), Phys. Rev. B 64 (2001), 035405, https://doi.org/10.1103/PhysRevB.64.035405.
[177] E. Voloshina, N. Berdunov, Y. Dedkov, Restoring a nearly free-standing character of graphene on ru(0001) by oxygen intercalation, Sci. Rep. 6. doi:10.1038/srep20285.
[178] J. Mao, L. Huang, Y. Pan, M. Gao, J. He, H. Zhou, H. Guo, Y. Tian, Q. Zou, L. Zhang, H. Zhang, Y. Wang, S. Du, X. Zhou, A.H. Castro Neto, H.-J. Gao, Silicon layer intercalation of centimeter-scale, epitaxially grown monolayer graphene on ru(0001), Appl. Phys. Lett. 100 (2012), 093101, https://doi.org/10.1063/1.3687190.
[179] C.L. Kane, E.J. Mele, Quantum spin hall effect in graphene, Phys. Rev. Lett. 95 (2005), 226801, https://doi.org/10.1103/PhysRevLett.95.226801.
[180] F. Calleja, H. Ochoa, M. Garnica, S. Barja, J.J. Navarro, A. Black, M.M. Otrokov, E. V. Chulkov, A. Arnau, A.L. Vázquez de Parga, F. Guinea, R. Miranda, Spatial variation of a giant spin–orbit effect induces electron confinement in graphene on pb islands, Nat. Phys. 11 (2014) 43–47, https://doi.org/10.1038/nphys3173.
[181] A.J. Martínez-Galera, J.M. Gómez-Rodríguez, Surface diffusion of simple organic molecules on graphene on pt(111), J. Phys. Chem. C 115 (2011) 23036–23042, https://doi.org/10.1021/jp208026u.
[182] A.J. Martínez-Galera, J.M. Gómez-Rodríguez, Nucleation and growth of the prototype azabenzene 1,3,5-triazine on graphite surfaces at low temperatures, J. Phys. Chem. C 115 (2011) 11089–11094, https://doi.org/10.1021/jp200613c.
[183] W. Dou, S. Huang, R.Q. Zhang, C.S. Lee, Molecule-ssubstrate interaction channels of metal-phthalocyanines on graphene on ni(111) surface, J. Chem. Phys. 134 (2011), 094705, https://doi.org/10.1063/1.3561398.
[184] J. Uihlein, H. Peisert, M. Glaser, M. Polek, H. Adler, F. Petraki, R. Ovsyannikov, M. Bauer, T. Chassé, Communication: influence of graphene interlayers on the interaction between cobalt phthalocyanine and ni(111), J. Chem. Phys. 138 (2013), 081101, https://doi.org/10.1063/1.4793523.
[185] S.J. Altenburg, M. Lattelais, B. Wang, M.-L. Bocquet, R. Berndt, Reaction of phthalocyanines with graphene on ir(111), J. Am. Chem. Soc. 137 (2015) 9452–9458, https://doi.org/10.1021/jacs.5b05558.
[186] R. Hoffmann, R.B. Woodward, Selection rules for concerted cycloaddition reactions, J. Am. Chem. Soc. 87 (1965) 2046–2048, https://doi.org/10.1021/ja01087a034.
[187] V. Corradini, A. Candini, D. Klar, R. Biagi, V. De Renzi, A. Lodi Rizzini, N. Cavani, U. del Pennino, S. Klyatskaya, M. Ruben, E. Velez-Fort, K. Kummer, N.B. Brookes, P. Gargiani, H. Wende, M. Affronte, Probing magnetic coupling between lnpc2 (ln = tb, er) molecules and the graphene/ni (111) substrate with and without au-intercalation: role of the dipolar field, Nanoscale 10 (2018) 277–283, https://doi.org/10.1039/C7NR06610D.
[188] M. Garnica, F. Calleja, A.L. Vázquez de Parga, R. Miranda, Mapping spin distributions in electron acceptor molecules adsorbed on nanostructured graphene by the kondo effect, Surf. Sci. 630 (2014) 356–360, https://doi.org/10.1016/j.susc.2014.07.028.
[189] A. Kumar, K. Banerjee, M. Dvorak, F. Schulz, A. Harju, P. Rinke, P. Liljeroth, Charge-transfer-driven nonplanar adsorption of f4tcnq molecules on epitaxial graphene, ACS Nano 11 (5) (2017) 4960–4968, https://doi.org/10.1021/acsnano.7b01599.
[190] J. Kondo, Resistance minimum in dilute magnetic alloys, Prog. Theor. Phys. 32 (1964) 37–49, https://doi.org/10.1143/PTP.32.37.
[191] M. Garnica, D. Stradi, F. Calleja, S. Barja, C. Díaz, M. Alcamí, A. Arnau, A.L.V. de Parga, F. Martín, R. Miranda, Probing the site-dependent kondo response of nanostructured graphene with organic molecules, Nano Lett. (2014) 4560doi, https://doi.org/10.1021/nl501584v.
[192] N. Lipari, C. Duke, R. Bozio, A. Girlando, C. Pecile, A. Padva, Electron-molecular-vibration coupling in 7,7,8,8-tetracyano-p-quinodimethane (tcnq), Chem. Phys. Lett. 44 (1976) 236–240, https://doi.org/10.1016/0009-2614(76)80498-8.
[193] H.T. Zhou, J.H. Mao, G. Li, Y.L. Wang, X.L. Feng, S.X. Du, K. Müllen, H.-J. Gao, Direct imaging of intrinsic molecular orbitals using two-dimensional, epitaxially-grown, nanostructured graphene for study of single molecule and interactions, Appl. Phys. Lett. 99 (2011), 153101, https://doi.org/10.1063/1.3646406.
[194] H. Zhou, L. Zhang, J. Mao, L. Geng, Y. Zhang, Y. Wang, S. Du, W.A. Hofer, H.-J. Gao, Template-directed assembly of pentacene molecules on epitaxial graphene on ru(0001), Nano Res. 6 (2013) 131–137, https://doi.org/10.1007/s12274-013-0288-8.
[195] S. Barja, M. Garnica, J.J. Hinarejos, A.L. Vázquez de Parga, N. Martín, R. Miranda, Self-organization of electron acceptor molecules on graphene, Chem. Commun. 46 (2010) 8198–8200, https://doi.org/10.1039/C0CC02675A.
[196] D. Maccariello, M. Garnica, M.A. Niño, C. Navio, P. Perna, S. Barja, A.L. Vázquez de Parga, R. Miranda, Spatially resolved, site-dependent charge transfer and induced magnetic moment in tcnq adsorbed on graphene, Chem. Mater. 26 (2014) 2883–2890, https://doi.org/10.1021/cm5005467.
[197] M. Garnica, D. Stradi, S. Barja, F. Calleja, C. Díaz, M. Alcamí, N. Martín, A. Vázquez de Parga, F. Martín, R. Miranda, Long-range magnetic order in a purely organic 2d layer adsorbed on epitaxial graphene, Nat. Phys. 9 (2013) 368, https://doi.org/10.1038/NPHYS2610.
[198] A.J. Pollard, E.W. Perkins, N.A. Smith, A. Saywell, G. Goretzki, A.G. Phillips, S. P. Argent, H. Sachdev, F. Muller, S. Hufner, S. Gsell, M. Fischer, M. Schreck, J. Osterwalder, T. Greber, S. Berner, N. Champness, P. Beton, Supramolecular assemblies formed on an epitaxial graphene superstructure, Angew. Chem. Int. Ed. 49 (2010) 1794–1799, https://doi.org/10.1002/anie.200905503.
[199] A.J. Martínez-Galera, N. Nicoara, J.I. Martínez, Y.J. Dappe, J. Ortega, J. M. Gómez-Rodríguez, Imaging molecular orbitals of ptcda on graphene on pt (111): electronic structure by stm and first-principles calculations, J. Phys. Chem. C 118 (2014) 12782–12788, https://doi.org/10.1021/jp500768y.
[200] M. Roos, B. Uhl, D. Kunzel, H.E.H.A. Gross, R.J. Behm, Intermolecular vs molecule-substrate interactions: a combined stm and theoretical study of supramolecular phases on graphene/ru(0001), Beilstein J. Nanotechnol. 2 (2011) 365–373, https://doi.org/10.3762/bjnano.2.42.
[201] M. Roos, D. Künzel, B. Uhl, H.-H. Huang, O. Brandao Alves, H.E. Hoster, A. Gross, R.J. Behm, Hierarchical interactions and their influence upon the adsorption of organic molecules on a graphene film, J. Am. Chem. Soc. 133 (2011) 9208–9211, https://doi.org/10.1021/ja2025855.
[202] J. Li, L. Solianyk, N. Schmidt, B. Baker, S. Gottardi, J.C. Moreno Lopez, M. Enache, L. Monjas, R. van der Vlag, R.W.A. Havenith, A.K.H. Hirsch, M. Stohr, Low-dimensional metal-organic coordination structures on graphene, J. Phys. Chem. C 123 (2019) 12730–12735, https://doi.org/10.1021/acs.jpcc.9b00326.
[203] N. Schmidt, J. Li, S. Gottardi, J.C. Moreno-Lopez, M. Enache, L. Monjas, R. van der Vlag, R.W.A. Havenith, A.K.H. Hirsch, M. Stohr, Comparing the self-assembly of sexiphenyl-dicarbonitrile on graphite and graphene on cu(111), Chem. Eur J. 25 (2019) 5065–5070, https://doi.org/10.1002/chem.201806312.
[204] J. Li, S. Gottardi, L. Solianyk, J.C. Moreno-Lopez, M. Stohr, 1,3,5-benzenetribenzoic acid on cu(111) and graphene/cu(111): a comparative stm study, J. Phys. Chem. C 120 (2016) 18093–18098, https://doi.org/10.1021/acs.jpcc.6b05541.
[205] P. Järvinen, S.K. Hämäläinen, M. Ijäs, A. Harju, P. Liljeroth, Self-assembly and orbital imaging of metal phthalocyanines on a graphene model surface, J. Phys. Chem. C 118 (2014) 13320–13325, https://doi.org/10.1021/jp504813v.
[206] J. Mao, H. Zhang, Y. Jiang, Y. Pan, M. Gao, W. Xiao, H.-J. Gao, Tunability of supramolecular kagome lattices of magnetic phthalocyanines using graphene-based moire patterns as templates, J. Am. Chem. Soc. 131 (2009) 14136–14137, https://doi.org/10.1021/ja904907z.
[207] H. Zhang, W. Xiao, J. Mao, H. Zhou, G. Li, Y. Zhang, L. Liu, S. Du, H.-J. Gao, Host-guest superstructures on graphene-based kagome lattice, J. Phys. Chem. C 116 (2012) 11091–11095, https://doi.org/10.1021/jp3020244.
[208] K. Banerjee, A. Kumar, F.F. Canova, S. Kezilebieke, A.S. Foster, P. Liljeroth, Flexible self-assembled molecular templates on graphene, J. Phys. Chem. C 120 (2016) 8772–8780, https://doi.org/10.1021/acs.jpcc.6b01638.
[209] I. Syôzi, Statistics of kagomé lattice, Prog. Theor. Phys. 6 (1951) 306–308, https://doi.org/10.1143/ptp/6.3.306.
[210] K. Yang, W.D. Xiao, Y.H. Jiang, H.G. Zhang, L.W. Liu, J.H. Mao, H.T. Zhou, S. X. Du, H.-J. Gao, Molecule-substrate coupling between metal phthalocyanines and epitaxial graphene grown on ru(0001) and pt(111), J. Phys. Chem. C 116 (2012) 14052–14056, https://doi.org/10.1021/jp304068a.
[211] H.G. Zhang, J.T. Sun, T. Low, L.Z. Zhang, Y. Pan, Q. Liu, J.H. Mao, H.T. Zhou, H. M. Guo, S.X. Du, F. Guinea, H.-J. Gao, Assembly of iron phthalocyanine and pentacene molecules on a graphene monolayer grown on ru(0001), Phys. Rev. B 84 (2011), 245436, https://doi.org/10.1103/PhysRevB.84.245436.
[212] M. Scardamaglia, S.L.G. Forte, A. Baraldi, P. Lacovig, R. Larciprete, C. Mariani, M. G. Betti, Metal-phthalocyanine array on the morié pattern of a graphene sheet, J. Nano Res. 13 (2011) 6013–6020, https://doi.org/10.1007/s11051-011-0384-1.
[213] S. Lisi, P. Gargiani, M. Scardamaglia, N.B. Brookes, V. Sessi, C. Mariani, M. G. Betti, Graphene-induced magnetic anisotropy of a two-dimensional iron phthalocyanine network, J. Phys. Chem. Lett. 6 (2015) 1690–1695, https://doi.org/10.1021/acs.jpclett.5b00260.
[214] M. Scardamaglia, S. Lisi, S. Lizzit, A. Baraldi, R. Larciprete, C. Mariani, M.G. Betti, Graphene-induced substrate decoupling and ideal doping of a self-assembled iron-

phthalocyanine single layer, J. Phys. Chem. C 117 (2013) 3019–3027, https://doi.org/10.1021/jp308861b.
[215] W. Dou, Q. Yang, C.-S. Lee, Anisotropic film growth of iron-phthalocyanine on graphene on a ni(111) substrate: roles of molecule-substrate and intermolecular interaction, Appl. Phys. Lett. 102 (2013), 131606, https://doi.org/10.1063/1.4800235.
[216] S.K. Hamalainen, M. Stepanova, R. Drost, P. Liljeroth, J. Lahtinen, J. Sainio, Self-assembly of cobalt-phthalocyanine molecules on epitaxial graphene on ir(111), J. Phys. Chem. C 116 (2012) 20433–20437, https://doi.org/10.1021/jp306439h.
[217] Y. Cai, H. Zhang, J. Song, Y. Zhang, S. Bao, P. He, Adsorption properties of copc molecule on epitaxial graphene/ru(0001), Appl. Surf. Sci. 327 (2015) 517–522, https://doi.org/10.1016/j.apsusc.2014.11.184.
[218] G. Li, H.T. Zhou, L.D. Pan, Y. Zhang, J.H. Mao, Q. Zou, H.M. Guo, Y.L. Wang, S. X. Du, H.-J. Gao, Self-assembly of c60 monolayer on epitaxially grown, nanostructured graphene on ru(0001) surface, Appl. Phys. Lett. 100 (2012), 013304, https://doi.org/10.1063/1.3673830.
[219] J. Lu, P.S.E. Yeo, Y. Zheng, Z. Yang, Q. Bao, C.K. Gan, K.P. Loh, Using the graphene moire pattern for the trapping of c60 and homoepitaxy of graphene, ACS Nano 6 (1) (2012) 944–950, https://doi.org/10.1021/nn204536e.
[220] M. Jung, D. Shin, S.-D. Sohn, S.-Y. Kwon, N. Park, H.-J. Shin, Atomically resolved orientational ordering of c60 molecules on epitaxial graphene on cu(111), Nanoscale 6 (2014) 11835–11840, https://doi.org/10.1039/C4NR03249G.
[221] D. Stradi, S. Barja, C. Díaz, M. Garnica, B. Borca, J.J. Hinarejos, D. Sánchez-Portal, M. Alcamí, A. Arnau, A.L. Vázquez de Parga, R. Miranda, F. Martín, Lattice-matched versus lattice-mismatched models to describe epitaxial monolayer graphene on ru(0001), Phys. Rev. B 88 (2013), 245401, https://doi.org/10.1103/PhysRevB.88.245401.
[222] S. Koch, D. Stradi, E. Gnecco, S. Barja, S. Kawai, C. Díaz, M. Alcamí, F. Martín, A. L. Vázquez de Parga, R. Miranda, T. Glatzel, E. Meyer, Elastic response of graphene nanodomes, ACS Nano 7 (2013) 2927–2934, https://doi.org/10.1021/nn304473r.
[223] C.G. Ayani, M. Pisarra, J.I. Urgel, J.J. Navarro, C. Díaz, H. Hayashi, H. Yamada, F. Calleja, R. Miranda, R. Fasel, F. Martín, A.L. Vázquez de Parga, Efficient photogeneration of nonacene on nanostructured graphene, Nanoscale Horiz 6 (2021) 744–750, https://doi.org/10.1039/D1NH00184A.
[224] N. Schmidt, J. Li, S. Gottardi, J.C. Moreno-Lopez, M. Enache, L. Monjas, R. van der Vlag, R.W.A. Havenith, A.K.H. Hirsch, M. Stöhr, On-surface light-induced generation of higher acenes and elucidation of their open-shell character, Nat. Commun. 10 (2019) 861, https://doi.org/10.1038/s41467-019-08650-y.
[225] M. Corso, W. Auwarter, M. Muntwiler, A. Tamaj, T. Greber, J. Osterwalder, Boron nitride nanomesh, Science 303 (2004) 217, https://doi.org/10.1126/science.1091979.
[226] H. Guo, A. J. Martínez-Galera, J. M. Gómez-Rodríguez, C_{60} self-orientation on hexagonal boron nitride induced by intermolecular coupling, Nanotechnology 32 (2021) 025711. doi:10.1088/1361-6528/abbbb2.
[227] H. Cun, A.P. Seitsonen, S. Roth, S. Decurtins, S.-X. Liu, J. Osterwalder, T. Greber, An electron acceptor molecule in a nanomesh: F4tcnq on h-bn/rh(111), Surf. Sci. 678 (2018) 183–188, https://doi.org/10.1016/j.susc.2018.04.026.
[228] S. Joshi, F. Bischoff, R. Koitz, D. Ecija, K. Seufert, A.P. Seitsonen, J. Hutter, K. Diller, J.I. Urgel, H. Sachdev, J.V. Barth, W. Auwärter, Control of molecular organization and energy level alignment by an electronically nanopatterned boron nitride template, ACS Nano 8 (2014) 430–442, https://doi.org/10.1021/nn406024m.
[229] J.I. Urgel, M. Schwarz, M. Garnica, D. Stassen, D. Bonifazi, D. Ecija, J.V. Barth, W. Auwarter, Controlling coordination reactions and assembly on a cu(111) supported boron nitride monolayer, J. Am. Chem. Soc. 137 (2015) 2420–2423, https://doi.org/10.1021/ja511611r.
[230] F. Schulz, R. Drost, S.K. Hämäläinen, P. Liljeroth, Templated self-assembly and local doping of molecules on epitaxial hexagonal boron nitride, ACS Nano 7 (2013) 11121–11128, https://doi.org/10.1021/nn404840h.
[231] D.A. Estyunin, I.I. Klimovskikh, V.Y. Voroshnin, D.M. Sostina, L. Petaccia, G. Di Santo, A.M. Shikin, Intrinsically patterned two-dimensional materials for selective adsorption of molecules and nanoclusters, Nat. Mater. 16 (2017) 717, https://doi.org/10.1038/NMAT4915.